Computational modeling and quantitative cell physiology reveal central parameters for the brassinosteroid-regulated cell growth of the *Arabidopsis* root

Ruth Großeholz[1,2†], Friederike Wanke[3†], Nina Glöckner[3†], Luiselotte Rausch[3], Leander Rohr[3], Stefan Scholl[1], Emanuele Scacchi[3], Amelie-Jette Spazierer[3], Lana Shabala[4], Sergey Shabala[4,5], Karin Schumacher[1], Ursula Kummer[1,2*‡], Klaus Harter[3*‡]

***For correspondence:**
ursula.kummer@bioquant.uni-heidelberg.de (UK); klaus.harter@zmbp.uni-tuebingen.de (KH)

[†]These authors contributed equally to this work
[‡]These authors contributed equally to this work

[1]Centre for Organismal Studies, Heidelberg University, Germany; [2]BioQuant, Heidelberg University, Germany; [3]Center for Molecular Biology of Plants, University of Tübingen, Germany; [4]Tasmanian Institute for Agriculture, University of Tasmania, Australia; [5]International Research Centre for Environmental Membrane Biology, Foshan University, Foshan, China

Abstract Brassinosteroids (BR) are key hormonal regulators of plant development. However, whereas the individual components of BR perception and signaling are well characterized experimentally, the question of how they can act and whether they are sufficient to carry out the critical function of cellular elongation remains open. Here, we combined computational modeling with quantitative cell physiology to understand the dynamics of the plasma membrane (PM)-localized BR response pathway during the initiation of cell elongation in the epidermis of the *Arabidopsis* root tip. The model, consisting of ordinary differential equations, comprises the BR induced hyperpolarization of the PM, the acidification of the apoplast and subsequent cell wall swelling. We demonstrated that the competence of the root epidermal cells for the BR response predominantly depends on the amount and activity of H^+-ATPases in the PM. The model further predicted that an influx of cations is required to compensate for the shift of positive charges caused by the apoplastic acidification. A potassium channel was subsequently identified and experimentally characterized, fulfilling this function. Thus, we established the landscape of components and parameters capable of triggering and guiding cellular elongation through the fast response to BRs, a central process in plant development.

Introduction

Brassinosteroids (BRs) are plant steroid hormones that regulate a great variety of physiological and developmental processes including elongation growth as well as environmental adaptations (***Müssig et al., 2002***; ***Clouse, 2002***; ***Lv and Li, 2020***; ***Wolf, 2020***). To achieve this, BR signal transduction is closely linked with a multitude of other signaling pathways (***Lv and Li, 2020***).

The canonical sequence of BR perception and signal transduction, which also leads to cell elongation, is mediated by the plasma membrane (PM)-resident, nanocluster-organized receptor kinase brassinosteroid-insensitive 1 (BRI1) and its co-receptor BRI1-activating kinase 1 (BAK1) as central elements (***Lv and Li, 2020***; ***Wolf, 2020***). The binding of BR to the receptor´s extracellular domain results in the re-arrangement of several proteins in the BRI1 nanocluster. This involves the release of inhibitory mechanisms that include BRI1 kinase inhibitor 1 (BKI1) and BAK1-interacting receptor like kinase 3 (BIR3) and leads to an increased interaction of BRI1 with BAK1 followed by a variety of auto- and trans-phosphorylation events of their cytoplasmic domains. This cascade of events eventually results in the establishment of the fully active BRI1 receptor complex.

Once the active complex is established, the BR response splits into two distinct downstream pathways to trigger cell elongation (***Clouse, 2002***, ***2011***): A gene regulatory pathway leading to extensive transcriptional rearrangements that are realized *via* the kinase Brassinosteroid Insensitive 2 (BIN2), by the key transcription factors brassinazole resistant 1 (BZR1) and BR insensitive EMS suppressor 1 (BES1) (***Lv and Li, 2020***). The second, faster pathway takes place in PM-resident BRI1 nanoclusters and leads to the upregulation of the proton pumping ATPase (AHA) activity (Fig. 1) (***Caesar et al., 2011***). The enhanced activity of AHA results in the acidification of the apoplastic space, hyperpolarization of the PM's membrane potential (E_m), activation of low pH-dependent apoplastic enzymes, which finally weaken the wall´s rigidity, causing wall swelling and eventually the onset of cell elongation (***Elgass et al., 2009***; ***Caesar et al., 2011***; ***Witthöft et al., 2011***; ***Witthöft and Harter, 2011***; ***Palmgren et al., 1991***; ***Regenberg et al., 1995***; ***Baekgaard et al., 2005***; ***Phyo et al., 2019***). This sequence of signaling and reaction pathways allows for instance root cells in the elongation zone (EZ) to grow four times their size in the meristematic zone (MZ) with a growth rate of up to 0.7 µm min^{-1} (***Fasano et al., 2001***; ***Verbelen et al., 2006***).

While the activation of the pathway is well understood qualitatively, the information on the inactivation of the pathway is currently still sparse. The receptor BRI1 autophosphorylates at the residue S891, which inhibits the receptor activity (***Oh et al., 2012***). However, the time-scale of this phosphorylation is very slow, as it increases over the course of 12 h after stimulation with BR. The dephosphorylation of this site is even slower, as residual phosphorylations can be detected 5 d after inhibiting BR synthesis using brassinazole (***Oh et al., 2012***).

Despite the qualitative knowledge on the constituents, the BR perception and the canonical signaling events, the dynamics of the system as a whole have yet to be examined quantitatively (***Sankar et al., 2011***; ***van Esse et al., 2012***, ***2013a***,b; ***Allen and Ptashnyk, 2017***). Therefore, we employed computational modeling in combination with quantitative experimental data on the fast

BR response pathway in the PM, focusing on the epidermal cells of the *Arabidopsis* root tip as the epidermis limits the rate of elongation (***Hacham et al., 2011***). The root tip is an excellent model system for such a combined study because cells there first undergo a phase of cell division in the MZ followed by a phase of growth in the EZ. The boundary from the MZ to the EZ is represented by the transition zone (TZ). The formation of the TZ is characterized by the cytokinin-induced expression of the *AHA1* and *AHA2* genes as a precondition for cell elongation in the EZ (***Pacifici et al., 2018***). However BR is involved both in the control of both cell division and cell elongation in the different zones, apparently also adding to the specific functional competence and behavior of the cells along the axis of the root tip. However, the molecular determinants and processes establishing this competence and their link to the cytokinin-caused gradient of growth competence are poorly understood in terms of their quantitative dynamics. This lack of knowledge virtually provokes the implementation of computational modeling.

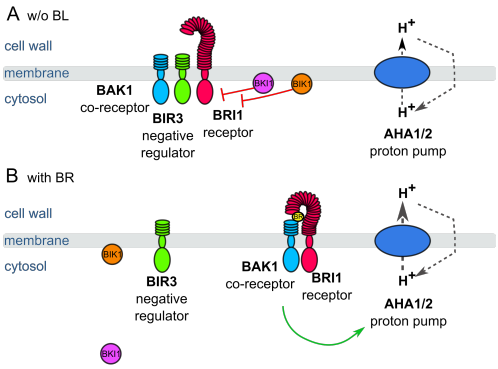

Figure 1. Schematic overview of the key constituents and processes of the plasma membrane-associated fast BR response pathway initiating early steps in cell elongation. A. Inactive state: Co-localizing in a preformed nanocluster, the inhibitors BKI1, BIK1 and BIR3 suppresses the activity of BRI1 in the absence of BR keeping the activity of H^+ ATPases AHA1 and 2 at basic levels. By interaction with BAK1, BIR3 blocks the access of the co-receptor to BRI1. B. Active state: Upon BR-binding to the receptor, the inhibitory mechanisms of BKI1, BIK1 and BIR3 on BRI1 and BAK1 are released causing the formation of the active BRI1/BAK1 complex. The complex enhances the AHA activity resulting in cell wall acidification, plasma membrane hyperpolarization and eventually onset of cell elongation. These key constituents and qualitatively described processes were used for the initial establishment of the computational model at cellular.

While computational modeling is commonly used in biomedical research, it has been used much less frequently in the plant field (***Hübner et al., 2011***; ***Holzheu and Kummer, 2020***). A few examples in plants include the modeling of auxin signaling (***Vernoux et al., 2011***) and transport pattern (***Band et al., 2014***), and parts of the BR signaling (***Sankar et al., 2011***; ***van Esse et al., 2012***, ***2013a***,b; ***Allen and Ptashnyk, 2017***). For instance, the modeling approach by van Esse *et al.* analyzed the link between the BR dose, gene expression and growth behavior in both the *Arabidopsis* root and shoot (***van Esse et al., 2012***, ***2013a***,b). However, none of the previous modeling approaches has been able to truly quantitatively depict cellular responses, make clear predictions about the cellular behavior or limiting constituents or processes.

In our study, we were able to determine how the constituents of the PM-resident fast BR response pathway work together and identified its rate-limiting elements applying an ordinary differential equations (ODE) approach. Substantiated by wet lab experiments, our computational approach led to a detailed kinetic model that describes the cellular response and explains the BR controlled differential growth behavior of the root cells on the basis of the differential AHA accumulation and activity. Furthermore, the model

predicted the existence of a cation influx across the PM that is crucial for the apoplastic acidification and E_m hyperpolarization - subsequently narrowed down experimentally. Lastly, the model shows of how the extent of the BR response can be fine-tuned by the level of the BIR3 inhibitor. Our model proposes that the specific composition of the PM-resident BRI1 nanoclusters determines the competence of the root cells to elongate in response to BR.

Results

A mathematical model of the fast BR response

To analyze the important steps and factors of the cell-specific, fast BR response in the root tip, we developed a detailed mathematical model consisting of ODEs (Fig. 2). The model comprises four cell compartments: the cytosol, the cell wall and the vacuole as three-dimensional compartments as well as the PM as a two-dimensional compartment. The explicit inclusion of the PM as two-dimensional compartment was prompted by the fact that most components of the BR perception and initial processes are located in the membrane and the relevance of the membrane as a scaling factor in this kind of system (***Holzheu et al., 2021***). The compartment sizes were set such that the model initially describes the behavior of a single epidermis cell in the early EZ of the *A. thaliana* root (***van Esse et al., 2011***) (see Appendix 1 Tab. 1).

The model captures the important components and steps of the fast BR response pathway. It is set up in a way that an equilibrium state was reached before the system is stimulated with the hormone by maintaining the system first without the hormone for 24 h. In this state, only a few crucial reactions occur and carry a flux (ν): the interaction between BIR3 and BAK1 (ν_7) and BIR3 and BRI1 (ν_6), the proton leak from the cell wall into the cytoplasm (ν_2), the basal activity of the ATPases AHA1 and AHA2 (ν_1) and the exchange of monovalent cations (here represented by potassium) between cytoplasm and cell wall (ν_4) and cytoplasm and vacuole (ν_5). Modeling the basal state as a physiologically plausible steady state ensures that the model describes the inactive state of the BR response pathway accurately and that the interactions of BIR3 with BAK1 and BRI1 are in an equilibrium.

The hormone is added to the model by an event triggered at 24 h. According to the current state of knowledge, this initiates a number of molecular processes in the PM that occur almost simultaneously (Fig. 2): binding of BR to BRI1 (ν_9), the loss of BRI1 inhibition by its C-terminus (ν_{12}), the release of BKI1 and BIK1 after phosphorylation (ν_{10} and ν_{11}, respectively) as well as the release of BIR3 from BAK1, the establishment of the BAK1-BRI1 interaction via BR (ν_{13}), and the auto- and transphosphorylation of BAK1 and BRI1 (ν_{14}). These spatial rearrangements and post-translational modifications result in the active form of the BRI1 receptor complex, which immediately stimulates the activity of H^+-ATPases very likely by phosphorylation (***Minami et al., 2019***) (ν_{15}). Further signaling events occur later in time and lead to differential gene expression (***Lv and Li, 2020***). However, these late events were not considered here for our modeling approach.

The main cell physiological output of this early sequence of events is the acidification of the apoplastic space,the swelling of the cell wall and the hyperpolarization of the E_m. The latter is calculated based on the net change in charge distribution of protons and potassium across the PM,

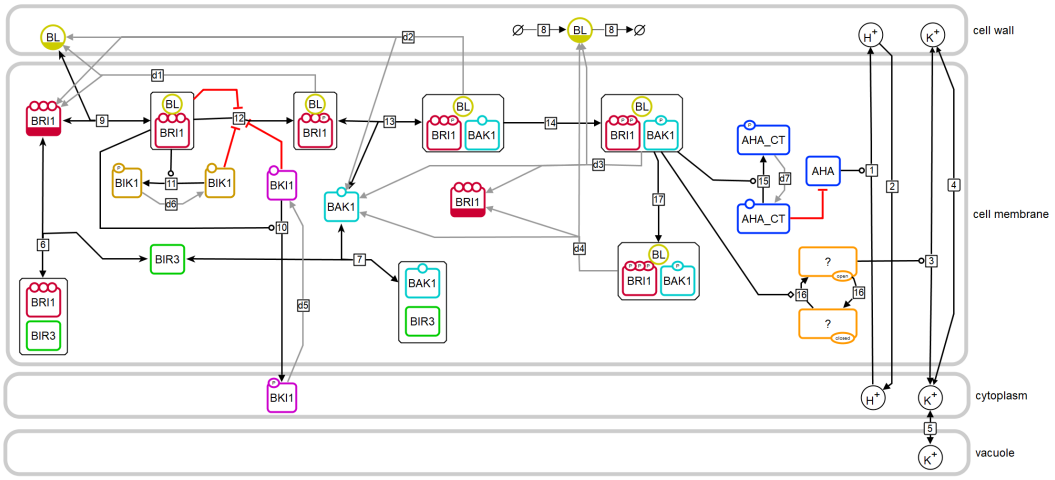

Figure 2. Model structure of the fast BR response pathway of *Arabidopsis thaliana*. Compartments are indicated by grey boxes. Smaller molecules are indicated by circles, proteins by rectangles. Potential sites for protein modifications are indicated by the small circles on the boundaries of the rectangles. Reactions, including substrates and products, are indicated by the arrows, with the reaction numbers noted in the small box. Reactions, which are required for the model to return to the initial state, are drawn in grey. A bar at the bottom of the circle or rectangle indicates that this entity appears more than once in the scheme.

the specific capacitance of the plasma membrane (***White et al., 1999***) and the membrane surface (***van Esse et al., 2011***) (see Appendix 1 Tab. 1). However, combining the available information derived from the literature resulted in preliminary model draft that was not able to reproduce the measured experimental data, for instance regarding the E_m hyperpolarization. Without a mechanism to balance out the shift in charge distribution caused by the transported protons, even a modest acidification of the apoplast from a pH of 5.4 to 5.0 will result in a membrane hyperpolarization greater than the one observed experimentally (***Caesar et al., 2011***) as we describe below in detail (see also: Appendix 1 - example calculation of E_m and pH change). Consequently, we postulated a cation channel in the model that opens upon activation of the BRI1 complex (v_{16}) and facilitates a monovalent cation influx (here represented by potassium) driven by the E_m (v_3).

In order to accurately model and simulate the fast BR response pathway, we therefore needed more experimental data about the PM-based BRI1 response module. Any remaining unknown model parameters were estimated based on the cell wall acidification (this study), E_m hyperpolarization (***Caesar et al., 2011***) and the qualitative overexpression behavior of BIR3 (***Imkampe et al., 2017***). To account for non-identifiable parameters, we investigated the parameter space by computing several independent model parameterizations that describe the experimental data equally well. All computational analyses were run with each model of the resulting ensemble of structurally identical models (n=10) to ascertain consistent results across parameter space.

Quantification of signaling components

One experimental challenge for the refinement of the model was to quantify the central components of the pathway comprising predominantly BRI1, BAK1, BIR3 and AHA in the PM of epidermal cells of the root tip. Initially, we drew our attention on their steady-state transcript levels as they

were determined by high-throughput single cell RNA-sequencing (scRNA-Seq) of the different *Arabidopsis* root cell types (**Ma et al., 2020**). Whereas *BRI1* and *BIR3* transcripts accumulated in all cell types of the root more or less equally and did not alter much in their amount during cell development along the root axis, *AHA2* and to much lower extent also *AHA1* transcripts were found predominantly in the epidermal cells and the root cortex (Fig. 3 A). During root development, the *AHA2* transcript amount but not those of *BRI1* and *BIR3* started to increase strongly in the cortex and epidermis cells of the TZ and EZ (Fig. 3 B). This temporal transcript pattern was less prominent for *AHA1* (Fig. 3 B) being in agreement with earlier observation that the *AHA1* promoter is not very active in root epidermis cells. This indicates that *AHA1* does not play a prominent role in the control of cell expansion (**Merlot et al., 2007**). Because its transcript accumulation was already induced by protoplasting, no scRNA-Seq data could be used for *BAK1* (**Ma et al., 2020**).

On the basis of the scRNA-Seq data we focused our further studies on the *in vivo* protein quantification of the GFP fusions of BRI1, BAK1, BIR3 and AHA2 in developing epidermal cells along the root tip axis. For the PM of cells of the early EZ, the amount of BRI1-GFP was already quantified to around 11 receptor molecules per μm^2 and for BAK1-GFP to 5 co-receptors per μm^2 for BAK1-GFP by **van Esse et al.** (**2011**). To complete this data set, we applied quantitative CLSM for the quantification of BIR3-GFP and AHA2-GFP in the epidermal root cells of published transgenic *Arabidopsis* lines that express the fusion protein under the respective native promoter (**Fuglsang et al., 2014**; **Imkampe et al., 2017**). As these GFP fusion proteins carry the identical fluorophore version, their fluorescence intensity can be set in relation to the BRI1-GFP intensity and, thus, to the BRI1-GFP receptor amount in the PM. The quantification of GFP fluorescence was performed in 50 x 50 µm areas at the epidermis along the root tip, as shown exemplarily in Fig. 3C. The amount of BRI1-GFP and BAK1-GFP did not alter much in the epidermal cells along the root axis, as it was reported before (Fig. 3 D) (**van Esse et al., 2011**). A relative homogeneous fluorescence intensity distribution was also observed for BIR3-GFP that translated to about 17 inhibitor molecules per μm^2 PM area in the MZ and 14 in the early EZ (Fig. 3 D). In contrast, there was a significant gradient of AHA2-GFP fluorescence intensity along the root axis, being comparatively low in the MZ (with 4 AHA2 molecules per μm^2 PM area) but high in the late EZ / maturation zone (with about 10 AHA2 molecules per μm^2 PM area) (Fig. 3 D). A relatively sharp alteration of the AHA2-GFP amount was detected for the TZ (Fig. 3 D). If the amount of AHA2-GFP and BIR3-GFP molecules was set in ratio to the number BRI1-GFP molecules in the PM along the root tip axis, there was no alteration with respect to BIR3 (ratio: about 1.35), but a strong increase regarding AHA2 from 0.28 in the MZ to up to 5 in the late EZ.

Our significantly improved spatio-temporal refinement of previous data (**Pacifici et al., 2018**) by scRNA-Seq and quantitative CLSM demonstrate a coincidence of AHA2 protein accumulation with the onset of growth in the EZ. These results suggest that the AHA2 protein accumulation and probably activity pattern may be regulatory related to normal and BR-regulated root growth along the root tip axis. This hypothesis is particularly plausible given that AHA2 interact physically with BRI1 and BAK1 *in vivo* (**Caesar et al., 2011**; **Ladwig et al., 2015**; **Yuan et al., 2018**).

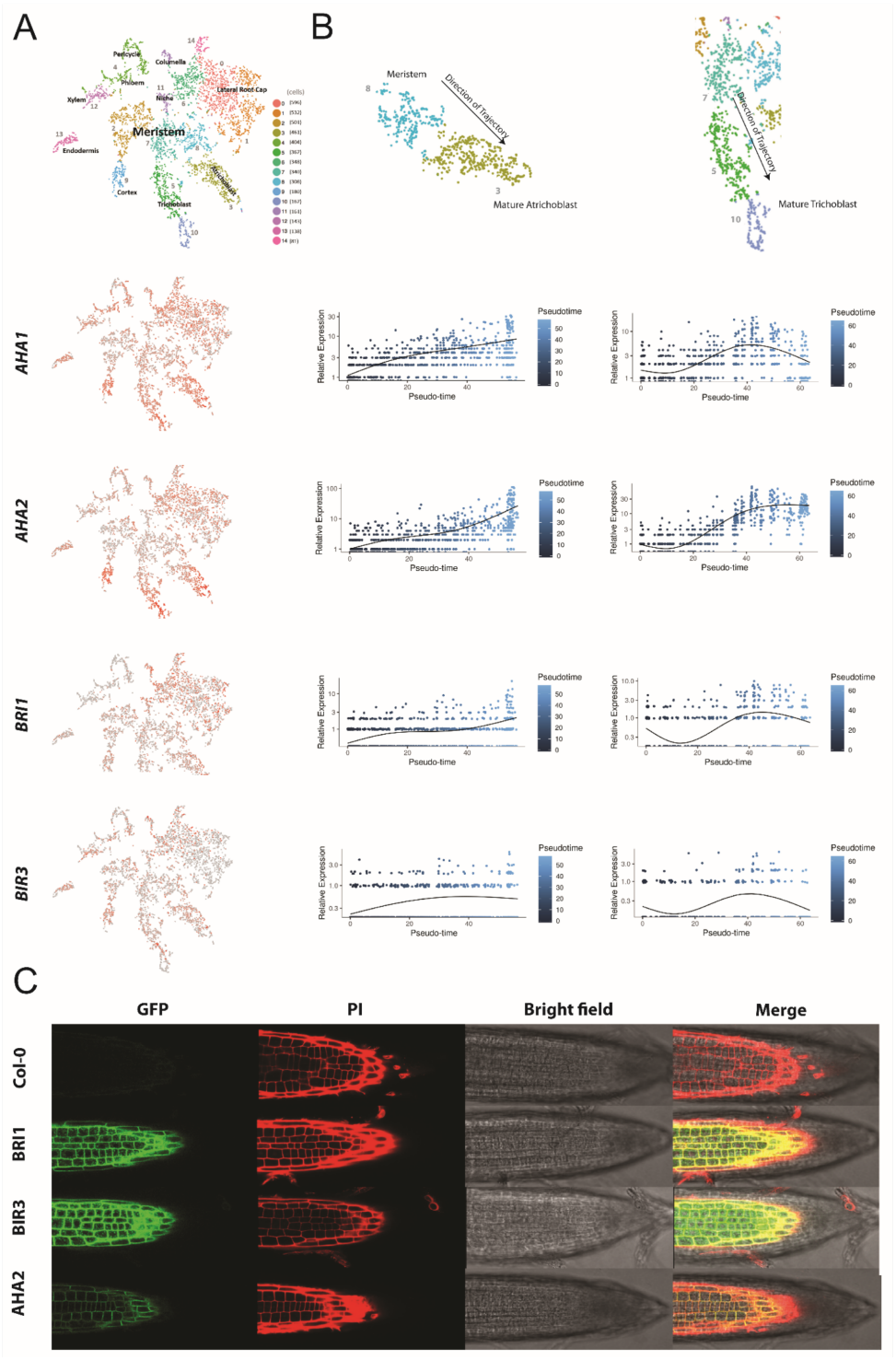

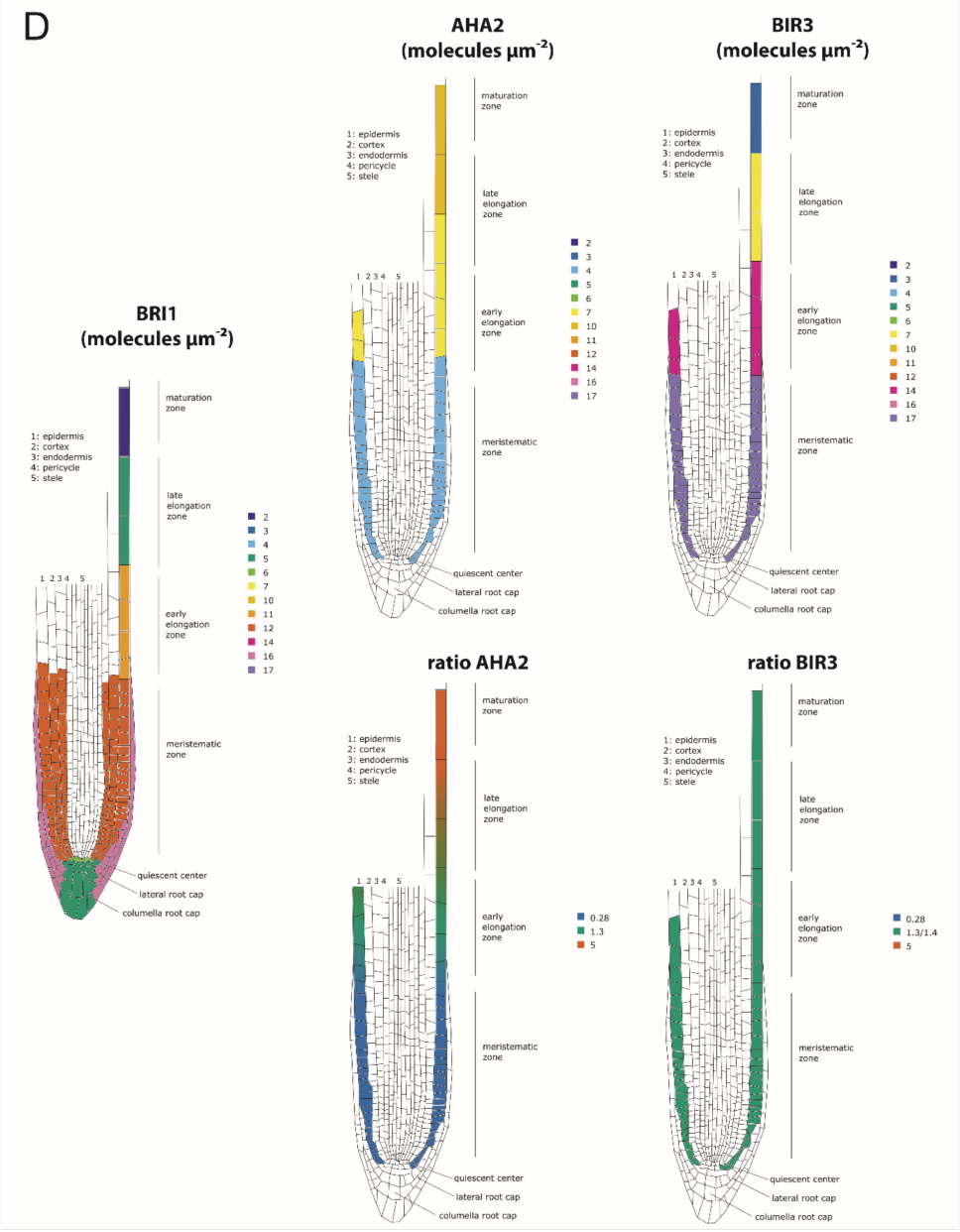

Figure 3. The constituents of the BRI1 nanocluster are spatio-temporally differentially expressed in the epidermal cells along the *Arabidopsis* root tip axis. A. *AHA1*, *AHA2*, *BIR3* and *BRI1* transcript levels in the different cell types of the *Arabidopsis* root tip derived from scRNA-Seq data (***Ma et al., 2020***). The atrichoblasts and trichoblasts together represent the epidermal cells. B. Developmental trajectories of *AHA1*, *AHA2*, *BIR3* and *BRI1* transcript accumulation along the root tip (***Ma et al., 2020***). The transition from the meristematic to the EZ is at a pseudotime value of around 30. C. Example of quantification of the GFP fluorescence of the AHA2, BIR3 and BRI1 fusion proteins, here in the plasma membrane of the meristematic region of the root epidermis in wild type *Arabidopsis* (Col-0 accession) and the respective transgenic lines. Left to right: GFP channel, PI channel, bright field, merged channels. The red box represents a 50 µm x 50 µm area chosen for the measurement here. D. *Upper panel*. Number of the indicated GFP fusion proteins (molecules per μm^2) in the plasma membrane of epidermal cells along the root tip axis. The values for BRI1-GFP and BAK1-GFP were taken from the literature (***van Esse et al., 2011***). *Lower panel*. The same but here the ratios of BRI1-GFP/AHA2-GFP and BRI1-GFP/BIR3-GFP molecules in the plasma membrane are given.

Modeling predicts the H^+-ATPases being crucial regulators of the extracellullar pH in the BR/BRI1 response

To test the hypothesis formulated above, we decided to investigate the functional role of AHA in the context of BR-regulated signaling activity both experimentally and computationally. Here, we first sought to quantify and analyze the response in the early EZ. With the key components of the H^+ homeostasis and nanocluster quantified, we were able to tailor the model to represent a single epidermis cell in the early EZ. By further using a combination of dose-response data and time-course measurements to fit the remaining unknown model parameters, we then should be able to analyze both the overall response and the temporal dynamics of the BR signaling module.

To measure the dose-response behavior and the time-course response to BR stimulation experimentally, we relied on the salt 8-hydroxypyrene-1,3,6-trisulfonic acid trisodium (HPTS), a non-invasive dye that incorporates into the plant cell wall and enables the ratiometric fluorescence readout of the pH conditions at cellular resolution (***Barbez et al., 2017***). To determine the apoplastic pH conditions 60 min after brassinolide (BL) application in the EZ, we performed a dose-response analysis. A significant decrease of the apoplastic pH was observed already at a BL concentration of 0.1 nM that continued up to a concentration of 10 nM (Fig. 4 A). Higher concentrations of BL did not further increase the cellular response in the EZ. This behavior is reproduced by the model ensemble (Fig. 4 A).

To capture not only the overall response to BL stimulation in the EZ but also its temporal dynamics, we further performed time-course measurements of the apoplastic pH in response to 10 nM BL using HPTS. Here, we observed a rapid acidification within 10 min of hormone application that is maintained for the remainder of the experiment (Fig.4 B). This observation was again reproduced by the model ensemble (Fig. 4 B). At the same time, we could also capture the cell wall swelling in the model that has been observed in response to BL application previously (***Elgass et al., 2009***; ***Caesar et al., 2011***) (Fig 4 C).

Using this model ensemble that specifically describes the behavior of a single epidermis cell in the early EZ, we analyzed the importance of the individual model components and parameters for the cell physiological response by calculating the scaled sensitivities. In particular, this means that we calculated the relative change of the cell wall acidification in response to relative changes in model parameters while simulating the BR response stimulated with 10 nM BL for 5 min and 60 min. The results of the sensitivity analysis for all model parameterizations (n = 10) are summarized in figure 5, where a positive influence on the BR response is denoted in green, no influence is denoted in white and a negative influence is denoted by red, with the color saturation indicating the strength of the control. Notably, at the beginning of the BR response the initial concentrations of the receptor BRI1 and the proton pumps have a large impact. In addition, parameters influencing proton extrusion such as the degree of inhibition and the pump activity of the ATPases strongly control the early BR response across all model parameterizations (Fig. 5). The sensitivities of the acidification 60 min after BL application in turn show a greater control of down-regulating elements such as the inhibitory phosphorylation of the receptor (Appendix 1 Figure 2), though the amount of proton pumps as well as their activity remain important. In combination with the quantifica-

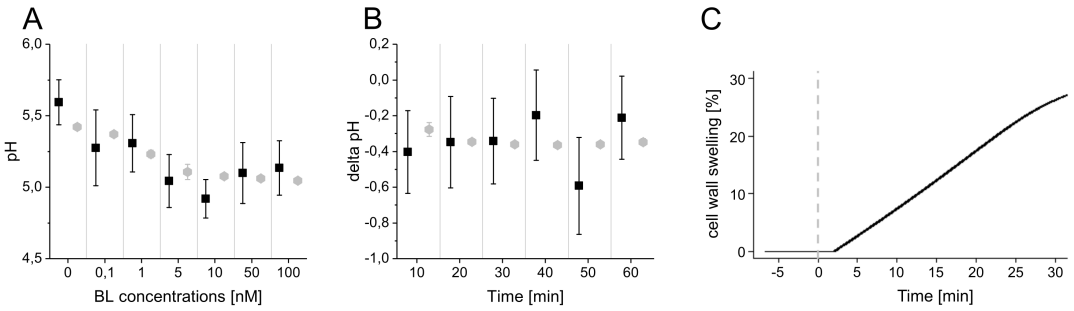

Figure 4. The computational model quantitatively and dynamically captures the sensitivity and kinetics of apoplastic acidification in *Arabidopsis* epidermal cells of the root early EZ in response to BL. A. HPTS-staining visualized (black quadrats) and computationally simulated (grey diamonds) dose-response behavior of apoplastic pH. Real or virtual BL incubation was done for 60 min. Error bars represent SE ($n \geq 14$) for the experimental data and SD for the simulations of different model parameterizations (n = 10). B. HPTS-staining visualized (black quadrats) and computationally simulated (grey diamonds) time-course of apoplastic pH change in response to 10 nM BL. Error bars represent SEM ($n \geq 16$) for the experimental data and SD for the simulations of different model parameterizations (n = 10). C. Computationally simulated time course of relative wall swelling in response to 10 nM BL. The virtual addition of BL at time 0 is indicated by the vertical dashed line.

tion data, this strongly supports our hypothesis that the proton pumps are the key elements that determine the competency of cells to respond to BR stimulation and react with elongation growth.

In consequence, the cells in the MZ should show a higher starting pH and react less strongly to BR stimulation due to the lower expression levels of AHA2. To predict the behavior of an epidermis cell in the MZ, we adjusted the model ensemble to instead represent a single epidermis cell in the MZ in terms of protein concentrations and compartment sizes. This model ensemble shows both a higher resting pH (Fig. 6 A) and a reduced response to BR stimulation as evident in the dose-response behavior that was confirmed experimentally by HPTS visualization (Fig. 6 B). At BL concentrations of 5 and 10 nM, the experimental pH values appear to be lower than those of the computational model (Fig. 6 A). This could indicate that further proton pumps besides AHA2 or other acidification mechanisms are activated by BL in the epidermal cells of the MZ.

Experimental evaluation confirm the predicted relevance of the H^+-ATPases for the extracellular pH control in the BR/BRI1 response

To confirm the predictions of the model experimentally, we used both HPTS and microelectrode ion flux estimation (MIFE) measurements, another non-invasive experimental method that allows for contact-free, real-time, electrophysiological measurements of H^+ fluxes at the surface of roots by using an H^+-specific electrode that mainly reflects the ATPase activity in the underlying tissues (***Newman, 2001***; ***Fuglsang et al., 2014***). Confirming previous results (***Staal et al., 2011***), our MIFE measurements along the Arabidopsis root tip revealed a net H^+ influx at the MZ, which then was drastically reduced in the EZ implying higher H^+ ATPase activity in this region (Fig. 7 A). These differential H^+ fluxes translate in a pH gradient along the surface of the root tip with the MZ less acidic and the elongation more acidic (***Staal et al., 2011***). Using HPTS, we could substantiate the

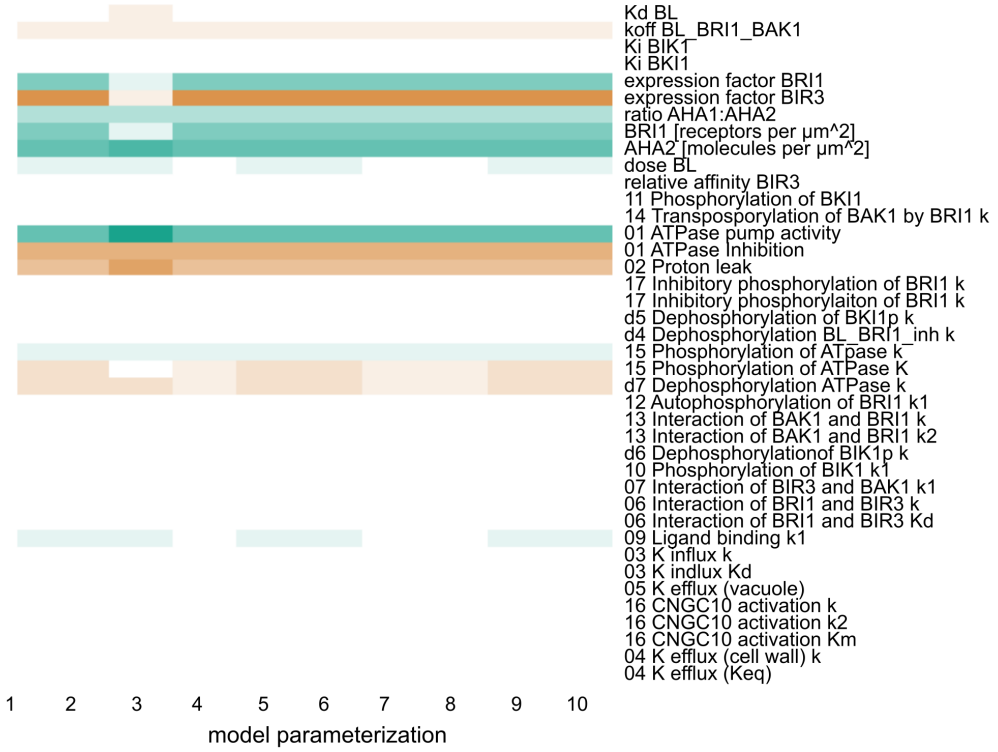

Figure 5. Computational calculation of scaled sensitivities of the cell wall acidification predicts AHA2 activity and molecules in the PM as well as BRI1 expression and molecules in the PM to be the deciding factors for the competence of *Arabidopsis* epidermal root cells to elongate in response to 5 min BL application for all parameterizations of the model. A positive influence is shown in green, a neutral in white and a negative in red, with the color saturation indicating the strength of the influence.

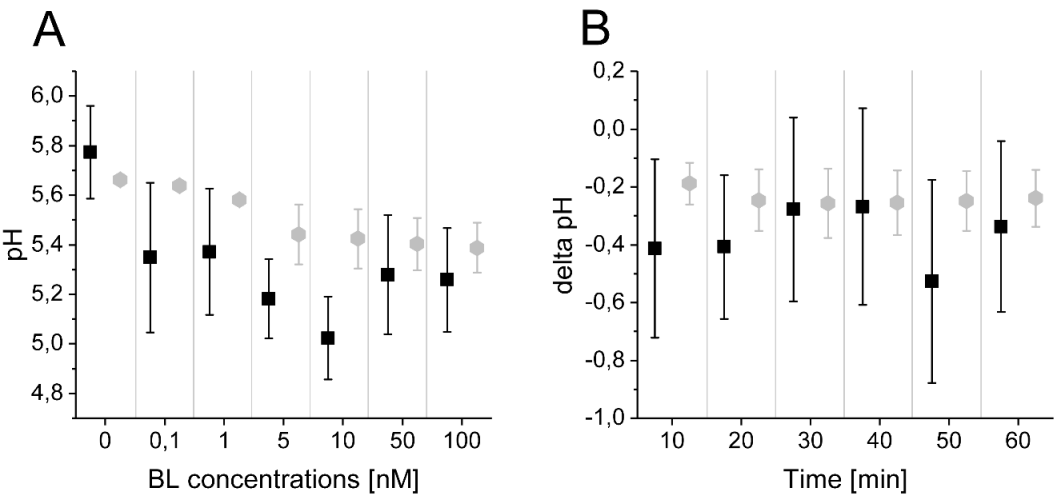

Figure 6. The computational model captures the sensitivity and kinetics of apoplastic acidification in *Arabidopsis* epidermal cells of the root MZ in response to BL. A. HPTS-staining visualized (black quadrats) and computationally simulated (grey diamonds) dose-response behavior of apoplastic pH. Experimental and virtual BL incubation was done for 60 min before HPTS measurements . Error bars represent SE ($n \geq 16$) in the experimental approach and SD for the simulations of different model parameterizations (n = 10). B. HPTS-staining visualized (black quadrats) and computationally simulated (grey diamonds) time-course of apoplastic pH change in response to 10 nM BL. Error bars bars represent SEM ($n \geq 16$) in the experimental approach and SD for the simulations of different model parameterizations (n = 10).

MIFE results and confirm the observation of ***Barbez et al.*** (***2017***) that there is an apoplastic pH gradient of the epidermal root cells from the MZ (less acidic) to the EZ (more acidic) (Fig. 7 B).

To address the question whether the establishment of the resting pH gradient and the differential changes of the pH conditions upon external BL application depend on fully functional BRI1, we used the *bri1-301* mutant for further HPTS and MIFE measurements. In the *bri1-301* mutant a BRI1 version with a reduced kinase activity is expressed, which causes a weak defective root growth phenotype at ambient temperature (***Lv et al., 2018***; ***Zhang et al., 2018***). This less-pronounced *bri1-301* phenotype allows HPTS and MIFE measurements technically comparable to those of wild type plants. As shown in figure 7 C, the BL-induced changes in the apoplastic pH observed for wild type were significantly lower in the *bri1-301* mutant. The HPTS data were again supported by our MIFE measurements: The wild type cells of the EZ showed an increase in the net H^+ efflux upon application of 10 nM BL, which continued over the measurement period of 20 min, whilst the cells of the *bri1-301* mutant responded much less (Fig. 7 D).

In summary, the concordant results of our experimental approaches substantiate the prediction of the mathematical model that the enhanced level of H^+ ATPase amount and activity in relation to the number of BRI1 receptors define the BR-regulated apoplastic acidification and linked hyperpolarization of the E_m. Moreover, the maintenance of the pH gradient and H^+ fluxes along the root tip axis and the BL regulation of alterations depend on kinase-active BRI1.

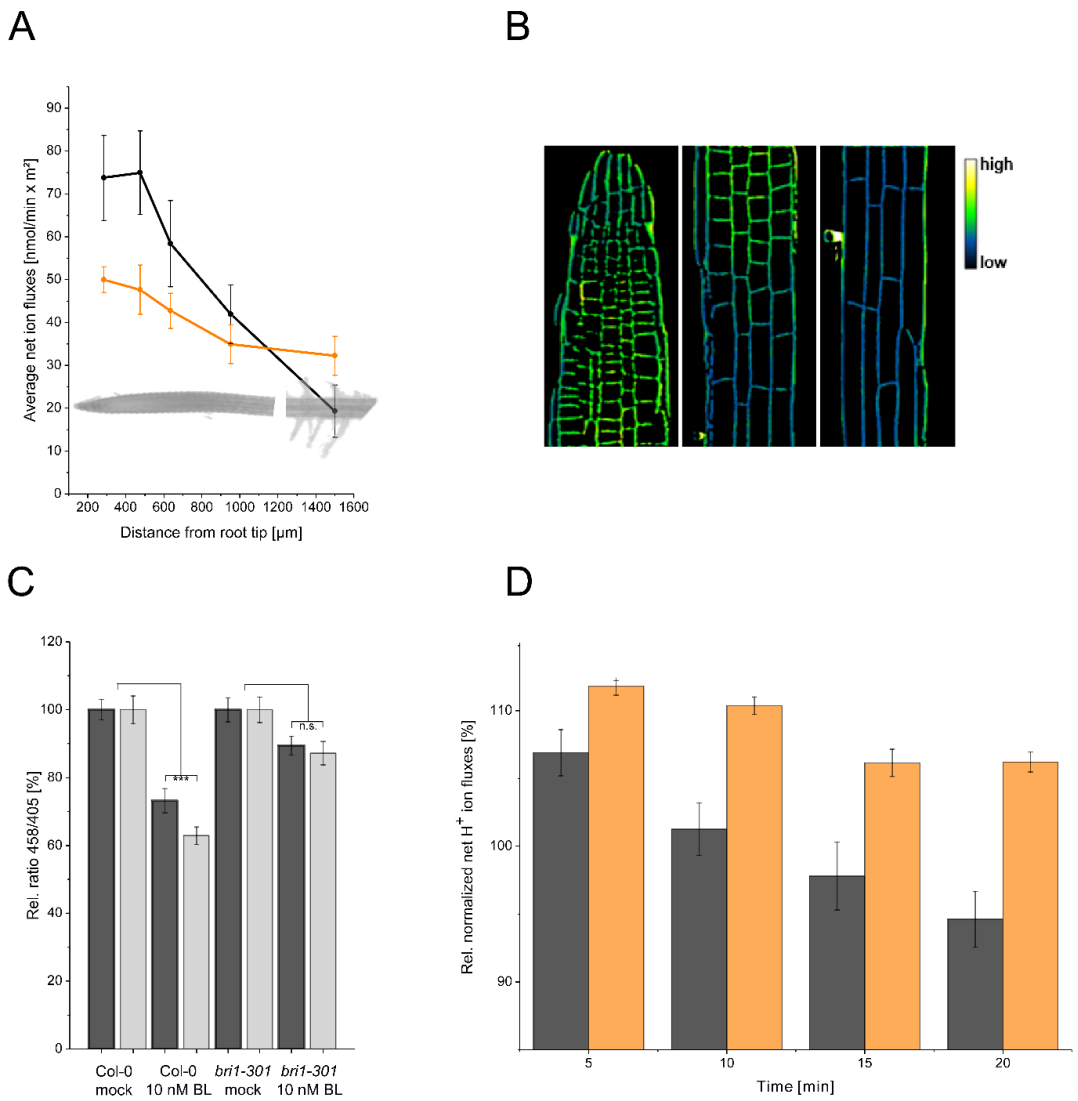

Figure 7. The resting apoplastic pH gradient of epidermal root cells along the axis and its regulation by BR depends on kinase-active BRI1. A. MIFE recording of the H^+ fluxes along the root axis of *Arabidopsis* wild type (black line) and *bri1-301* mutant (yellow line) plants. Measurements were performed every 100 µm from 250 µm of the root tip off to the root hair zone. Error bars represent SD (n = 3). B. Representative image of the apoplastic pH of epidermal cells along the root axis of wild type *Arabidopsis* using HPTS-staining starting with the MZ (left) over the TZ/early EZ (middle) to the late EZ (right). C. Comparison of the relative apoplastic pH (ratio 458/405) of epidermal root cells in the MZ (black bars) and EZ (grey bars) of wild type and *bri1-301* mutant plants after 60 min of BL (10 nM) or mock treatment, visualized by HPTS staining. The data derived from the mock treatments of the respective line were set to 100. Error bars represent SE. Statistical evaluations were performed by ANOVA followed by Tukey-Kramer HSD post hoc test. The black asterisks indicate statistically significant differences (***: $P < 0.001$); ns: not significant. D. Relative H^+ fluxes at the EZ of wild type (black bars) and *bri1-301* mutant (yellow bars) plants between 5 and 20 min after application of 10 nM BL recorded by MIFE. The flux directly before the addition of BL was set to 100. The increase in net influx after probe application is due to a disturbance of the H^+ conditions at the root surface, which is observed with any treatment.Error bars represent SD (n = 3).

Modeling predicts a cation channel for charge compensation during H^+ export and PM hyperpolarization

The great value of mathematical modeling and prediction is especially demonstrated after we calculated the membrane potential derived from the pH value changes in the apoplastic cell space of the root tip upon BL treatment and compared it with the previously experimentally determined E_m changes (***Caesar et al., 2011***). The calculated E_m change induced by the change in charge distribution due the acidification of the apoplastic space was much stronger as the measured one (Fig. 8 A and Appendix 1 - example calculation of E_m and pH change based on membrane area, specific membrane capacitance and transported charges): An acidification from pH 5.4 to pH 5.0 in response to 10 nM BL corresponds to a E_m change of approximately 28 mV, as opposed to the experimentally measured 7.2 mV (***Caesar et al., 2011***). According to the prediction of our model, this discrepancy values was eliminated, if an import of monovalent cations such as potassium (K^+), which predominantly contributes to the E_m of the PM in plant cells (***Higinbotham, 1973***), took place in parallel to the ATPase generated H^+ extrusion. Against the background that BAK1 and AHA2 interact with a cation channel of the cyclic nucleotide-gated ion channel (CNGC) family in the phytosulfokine receptor 1-mediated growth response (CNGC17; (***Ladwig et al., 2015***)), we searched in the literature and the Arabidopsis eFP browser (***Sullivan et al., 2019***) for a CNGC member, which is expressed in the root, localizes to the PM, imports K^+ ions, and is functionally linked to cell expansion, and identified CNGC10 (***Borsics et al., 2007***; ***Christopher et al., 2007***; ***Duszyn et al., 2019***). When CNGC10 and its K^+ transport properties were integrated into our model, the discrepancy between the calculated and measured value was gone (Fig. 8 B). This suggests that the CNGC10-mediated influx of potassium counteracts the ATPase-caused efflux of H^+ into the apoplast in the root tip.

To test whether CNGC10 is able to interact with components of the BRI1 nanocluster such as BRI1, BAK1 and AHA2, Förster resonance energy transfer by fluorescence lifetime imaging (FRET-FLIM) analyses in transiently transformed *Nicotiana benthamiana* leaf cells and yeast mating-based split-ubiquitin (mbSUS) assays were performed. The growth of yeast cells on interaction selective media and the reduction of the GFP fluorescence lifetime (FLT) revealed a spatially very close association (below 13 nm; (***Glöckner et al., 2020***)) and interaction, respectively, of CNGC10 with BRI1, BAK1 and AHA2 (Fig. 8 C-E). To test whether CNGC10 functions in the fast BR response pathway, we analyzed the BL-induced apoplastic pH change in two independent *cngc10* loss-of-function lines (***Jin et al., 2015***; ***Borsics et al., 2007***) compared to the corresponding wild type (Col-0). In contrast to the wild type both mutants did not acidify the apoplast of the cells in the EZ upon application of 10 nM BL (Fig. 8 F), whilst the mutant cells of the MZ behaved like wild type (Appendix 1 Fig. 3). These data indicate that CNGC10 is the major K^+ channel to maintain the E_m homeostasis of the PM during BL-induced apoplastic acidification primarily in the EZ and appears to be an additional constituent of the elongation growth-related BRI1 nanocluster.

Computational modeling enables the in silico analysis of BIR3 function

To further demonstrate the performance of our model, we investigated the function of the inhibitor BIR3 in the activity modulation of the BRI1 nanocluster in more detail *in silico*. The basis

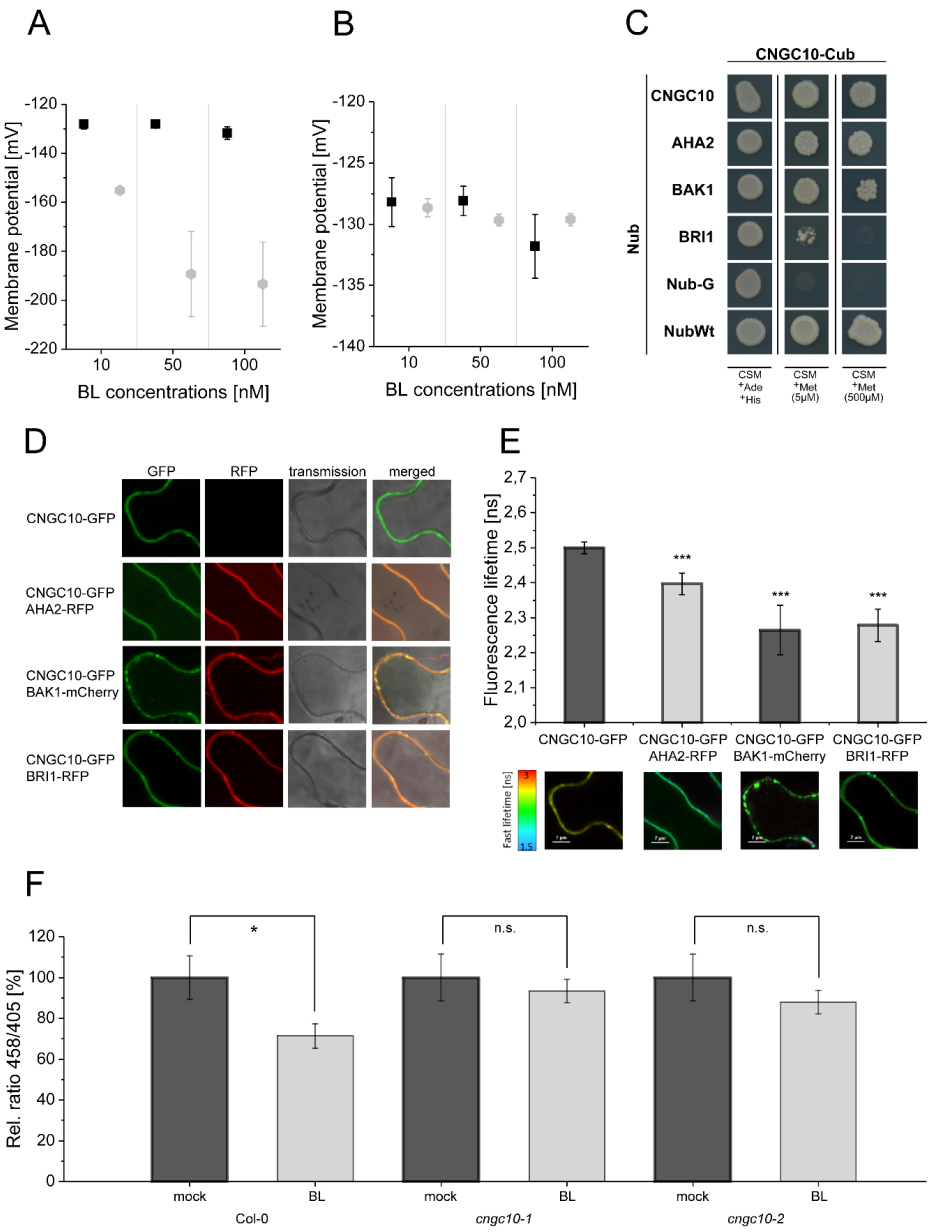

Figure 8. The computational model predicts the existence of a potassium channel, likely to be CNGC10, to maintain the homeostasis of the plasma membrane potential and apoplastic pH in *Arabidopsis* epidermal root cells of the early EZ. A. Modeled E_m in the presence of different different BL concentrations without the integration of potassium import (grey diamonds) in comparison to the published experimental data (black quadrats; ***Caesar et al.*** (***2011***)) after 20 min of BL treatment. B. Modeled E_m in the presence of different BL concentrations with the integration of the CNGC10 potassium channel (grey diamonds) in comparison to the published experimental data (black quadrats; ***Caesar et al.*** (***2011***)). Error bars in A and B represent SEM ($n \geq 4$) in the experimental approach and SD of simulation results of the different model parameterizations. C. CNGC10 forms homomers and interacts with BAK1 and AHA2 in the yeast mating-based split-ubiquitin system. The indicated combinations of Cub and Nub fusion constructs were transformed into yeast cells. Yeast cells were then grown either on media selective for the presence of the plasmids (CSM +Ade,+His) or on interaction selective media with two different concentrations (5 µM, 500 µM) of methionine (CSM +Met). The combination of CNGC10-Cub with Nub-G served as negative and that with NubWT as positive control. D. CNGC10 colocalizes with AHA2, BAK1 and BRI1 in the plasma membrane of plant cells. Representative confocal images of transiently transformed tobacco epidermal leaf cells expressing the indicated fusion proteins.

Figure 8. (continued) E. CNGC10 is spatially closely associated with AHA2, BAK1 and BRI1 in the plasma membrane of plant cells. Fluorescence lifetime imaging microscopy (FLIM) analysis comparing the different Förster resonance energy transfer (FRET) pairs. *Top*: FLIM measurements of transiently transformed tobacco epidermal leaf cells expressing the CNGC10-GFP donor fusion with the indicated RFP or mCherry acceptor fusions. Error bars indicate SD ($n \geq 21$). Statistical evaluations were performed by a Kruskal-Wallis test followed by Steel-Dwass post hoc test. The black asterisks indicate statistically significant differences (***: $P \leq 0.0001$). *Bottom*: Heat maps of representative plasma membrane areas used for FLIM measurements. The donor lifetimes of CNGC10 are color-coded according the scale at the left. F. Comparison of the relative apoplastic pH (ratio 458/405) of epidermal root cells in the EZ of wild type and two independent *cngc10* mutant plants after 60 min of BL (10 nM) or mock treatment, visualized by HPTS staining. The data derived from the mock treatments of the respective line were set to 100. Error bars represent SE ($n \geq 8$). Statistical evaluations were performed as described in Fig. 7C. The black asterisk indicates statistically significant differences (*: $P = 0.021$); n.s.: not significant.

for the focus on BIR3 were the observations by ***Imkampe et al.*** (***2017***) regarding the activity of the BR signaling in BIR3 as well as BIR3 and BRI1 overexpressing plant in the parameter estimation: The pathway should be inactive (= no acidification), when BIR3 is overexpressed, whilst the additional overexpression of BRI1 should restore the signaling activity to approximately normal levels. As shown in figure 9 A, the model was actually able to represent the BR activity of the respective growth-related phenotypes of *Arabidopsis* plants with altered BIR3 levels (***Imkampe et al., 2017***). Against this background we decided to investigate the behavior of different BIR3 expression levels in comparison to wild-type level in the root by analyzing the pH change 20 min after stimulation with 10 nM BL. As shown in the resulting expression-response curve (Fig. 9 B), the overall response decreased with increasing concentrations of BIR3 for all model parameterizations. This suggests that it is possible for the plant to fine-tune the signaling output by adjusting the expression level of the negative regulator BIR3. Finally, we also analyzed the dynamics of the overall pH response at different BIR3 accumulation levels, namely in the absence of BIR3, the normal protein amount of around 13 BIR3 molecules μm^{-2} PM and a 10- and 100-fold overaccumulation of BIR3. Here, the actual time-course behavior of the acidification varies between the different model parameterizations as the span of possible values deviated from the average pH response for the BIR3 expression (Fig. 9 C). Depending on the parameterization, it was possible for the model to either show a strong activation that tapered off or a more gradual response over the time- frame of an hour. For most model parameterizations, a 10-fold overexpression of BIR3 is sufficient to inactivate the BRI1 signaling module confirming the importance of the regulation by BIR3.

Discussion

BR fulfill a central role in regulating plant physiology, growth and development as well as adaption to the environment (***Lv and Li, 2020***). A prominent example for a BR function is the rapid initiation of the (epidermal) cell growth in the EZ but not in the MZ of the *Arabidopsis* root tip (***Lv and Li, 2020***). Evidently, the hormone implements on an already existing, functional competence of the root cells that, according to our experimental data, cannot be attributed to the absence of the BRI1/BAK1 perception system but must have other reasons. Moreover, although the main

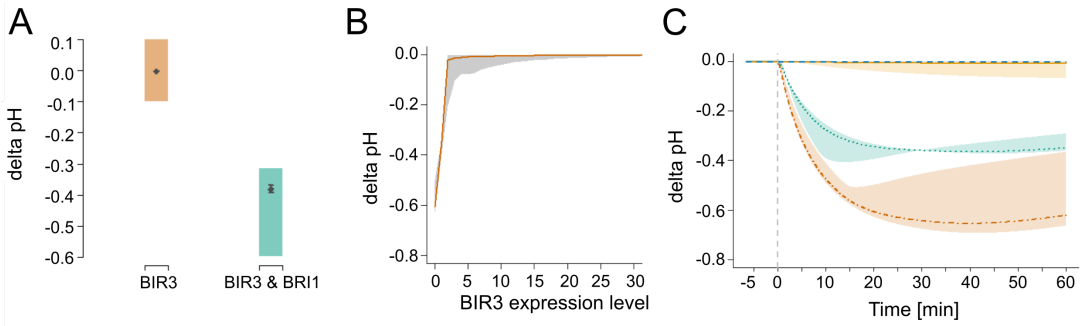

Figure 9. *In silico* analysis of the functional role of the negative regulator BIR3 on BL-regulated apoplastic acidification. A. Modelled qualitative acidification output of plants overexpressing BIR3 and BIR3&BRI1, respectively. The colored area represents the pH response targeted during parameter estimation, which was approximated by the activity of BR signaling indicated by the plant phenotypes (***Imkampe et al., 2017***). B. BIR3-Expression-response curve. Shown is the pH change 20 min after stimulation with 10 nM BL at different BIR3 expression levels ranging from 0- (loss-of-function mutant) to 30-times the normal expression level of the wild-type. The entire range of simulated responses is indicated by the shaded area, the averaged response of all models is denoted by the line. C. Exemplary time-course simulations of the pH change at 0 (loss-of-function mutant, orange), 1- (wild type expression, green), 10- (yellow) and 100-fold (blue) expression of BIR3 upon virtual application of 10 nM BL. Shown is the average pH response for the respective BIR3 expression level with the span between minimal and maximal values indicated by the colored area. The virtual addition of BL at time 0 is indicated by the vertical dashed line.

molecular determinants of BR perception and signaling are known, the processes leading to this competence and its realization towards, in this case, elongation were so far not well understood.

To address this problem we quantitatively analyzed the dynamics of the PM-resident fast BR response pathway as a whole by a recurring combination of computational modeling and wet lab experiments. The model´s predictions of the crucial constituents in the BRI1 nanocluster were experimentally verified, thereby determining the deciding and regulating elements for the signaling output. Using a detailed kinetic model on the basis of ODEs we could analyze the interplay of the signaling components and the system as a whole: We captured the dynamics of the apoplastic acidification and E_m hyperpolarization without BR and in response to the hormone. In addition, we showed that the rapidity and degree of the apoplast acidification in response to BR application is determined largely by the amount and activity of the ATPase AHA2 in the PM of the epidermal root cells. Furthermore, the model predicted that an influx of cations is required in order to explain both the pH and E_m changes of the PM simultaneously. We found that CNGC10 is the responsible cation (potassium) channel, as, besides functional evidence, it associates with BRI1, BAK1 and the proton pumps AHA2 *in vivo*. CNGC10 could therefore be another constituent of the BRI1 nanocluster in the PM of root cells. Lastly, we refined by computational modeling the putative regulatory role of BIR3 in the response pathway, as the signaling output can be in principle fine-tuned depending on the BIR3 level. Based on these results, we propose that the ongoing of the elongation growth, that involves altered gene expression later in time, is not possible if the initial rapid processes such as apoplast acidification, E_m hyperpolarization and charge compensation, which eventually lead to cell wall loosening followed by rapid wall swelling (***Elgass et al., 2009***; ***Caesar et al., 2011***), do not occur adequately.

If we project the measured AHA2 amount and AHA activity, and the apoplastic pH of epidermal cells along the axis of the root tip, we observe that they both increase and decrease, respectively, with the begin of the EZ and strongly correlate with the competence to grow upon BL application. Proposed by the computational model the AHA2s appear to be the rate-limiting factor for the cells to be able to respond to BR by elongation. The BR-mediated control of the H^+ ATPase and, thus, the E_m concerns not only elongation growth. The E_m is also central for adaptive responses to a broad range of abiotic cues and for developmental processes. Our observations therefore suggest that the regulation of H^+ ATPase contributes to the versatile functions of BR in all of these processes (***Lv and Li, 2020***; ***Wolf, 2020***).

Regardless, we are uniquely able to represent BR signaling activity *in silico* based on the cell physiological parameters (apoplastic pH, E_m of the PM, cell wall swelling) in a temporal and quantitative manner from the origin of a cell in the root apical meristem to its destination in the EZ. Most interestingly, the availability of especially AHA2 for its incorporation into the BRI1 nanocluster in the PM is built on the cytokinin-induced onset of *AHA* expression in the TZ (***Pacifici et al., 2018***). The positional information for the cytokinin function is, in turn, created by an auxin gradient along the root tip (***Pacifici et al., 2018***). Our results therefore show how a developmental gradient along the root tip, which is generated by the interplay of auxin and cytokinin, translates into the cell-specific competence for BR-regulated elongation growth.

As proposed recently, a further determinant of the cellularly different BR response appears to be a locally different BR biosynthesis and, thus, BR amount (***Vukasinovic et al., 2020***). Whereas low BR concentrations are optimal for the cellular activity in the MZ, high concentrations are required for the optimal cellular activity in the EZ. However, this concept cannot explain why the cells of the MZ hardly start to elongate independently of the BR concentration. As discussed above, we propose that either an increased proportion of AHA2 in the BRI1 nanoclusters or the increased number of AHA2-containing BRI1 nanoclusters are critical for establishing the differential competence of epidermal cells for (BR-regulated) growth along the root tip axis.

Varying the nanoclusters composition is an elegant way to achieve cell- and tissue-specific responses to a given cue when the number of available perception, signaling and output elements is limited. This principle also seems to be realized in various BRI1-mediated function. For example, the BRI1-dependent regulation of the vascular cell fate in the MZ of the root or the BRI1-mediated cross-tissue control of the cell wall homeostasis require BRI1 nanoclusters that contain at least additionally RLP44 (***Wolf et al., 2014***; ***Holzwart et al., 2018***). Moreover, RLP44-containing BRI1/BAK1 nanoclusters are spatially distinct from for instance FLS2/BAK1 nanoclusters (***Glöckner et al., 2020***).

The availability of a sophisticated model also enables *in silico* genetics that simplify the understanding of complex regulatory processes and their sometimes non-intuitive effects on the functional outputs. This is illustrated here by the example of the negative regulator BIR3 that prevents the interaction of BAK1 and BRI1 in the absence of the hormone thereby suppressing BR signaling (***Imkampe et al., 2017***; ***Großeholz et al., 2020***). Our computational model not only represents and predicts the BR activity of the growth-related phenotypes of the *Arabidopsis bir3* mutant and BIR3-overexpressing plants but also allows statements about the dose-dependent fine-tuning of BIR3 on BR/BRI1/BAK1-related functions. Such *in silico* genetic and physiological approaches can

be used to determine the functional and regulatory significance of other components of the fast BR response pathway as shown for AHA2 and the prediction of a cation channel for charge compensation. Thus, computational modeling facilitates the prioritization of the components of a perception and signaling system whose function should first be tested experimentally.

In summary, the recurrent application of computational modeling and subsequent wet lab experiments provided a novel in-depth and quantitative view of the initial cell physiological processes, regulatory networks and information processing leading to a minimal molecular and biochemical framework of the onset of BR-regulated elongation growth along the axis of the root tip. This approach can in principle be applied for the analysis of every signal perception and transduction process as long as a minimal set of elements and quantitative data are available or experimentally accessible.

The ongoing challenge will now be to establish a model of elongation growth across all tissues of the root tip. At the cellular level, the further aim is to integrate into the model the data of the potentially BR-modified composition, assembly and dynamics of the BRI1 nanocluster in the PM obtained by sophisticated super-resolution microscopy and *in vivo* FRET studies (***Glöckner et al., 2020***).

Methods and Materials

Experimental Methods

Plant Material

Seeds of the *Arabidopsis* mutants and lines expressing the different fusion proteins were surfaced sterilized and placed on ½ Murashige and Skoog (MS) medium plates with 1 % phytoagar and 1 % sucrose followed by stratification at 4° C in the dark for 2 days. Afterwards the plants were grown in growth chambers at 20° C under long day conditions (16 h light/8 h dark) for 5 days. The transgenic *Arabidopsis* lines (Col-0 ecotype) contained either a *pBRI1:BRI1-GFP* (wild type background; (***Friedrichsen, 2000***)), a *pAHA2:AHA2-GFP* (*aha2-4* mutant background; (***Fuglsang et al., 2014***)) or a *pBIR3:BIR3-GFP* construct (*bir3-2* background; (***Imkampe et al., 2017***)). The *Arabidopsis bri1-301* mutant (Col-0) was described in detail previously (***Lv et al.*** (***2018***); ***Zhang et al.*** (***2018***) and references therein).

Microelectrode ion flux estimation (MIFE) measurement

For MIFE measurements, 5-days-old seedlings were grown as described but in continuous light. Experiments were performed as described by ***Fuglsang et al.*** (***2014***). The seedlings were equilibrated in bath medium (0.1 mM $CaCl_2$, 0.5 mM KCl, pH 5.8) for 2 h before the measurements. Only seedlings without proton oscillations were used. At time point 0, 1 nM BL was added. The bathing solution was mixed two times by carefully pipetting up and down after addition of BL. The proximal position of the electrode (near the root) and the distal position (far from the root) were swapped compared to the previous study (***Fuglsang et al., 2014***). Consequently, a decrease in values represents proton efflux and an increase represents proton influx in our measurements.

8-Hydroxypyrene-1,3,6-trisulfonic acid trisodium salt (HPTS) measurement

For root apoplastic pH measurements, plates containing ½ MS agar media pH 5.7 without buffer, 1 mM HPTS dye, and the respective treatments were used. 5 days old *Arabidopsis* seedlings were transferred onto the media and treated for 60 min with HPTS prior to imaging. For shorter treatments, seedlings were prestained with HPTS and subsequently treated according to the indications. For imaging, the plants on the media were flipped into a nunc imaging chamber (Ibidi 80286), the roots being close to the chamber bottom and covered by the media. Ratiometric imaging was conducted at an inverted Zeiss LSM880 confocal scanning microscope. The 405nm and 458nm laser were used at 0.2% and 100% intensity respectively, a PMT detector range from 495 to 535 nm was used and line sequential scans were performed. The detector gain was set at 1200. For imaging, a 40x water immersion objective was used. The evaluation of ratio in the resulting images was determined following the workflow described by **Barbez et al.** (**2017**). For calibration curve measurements, ½MS agar media supplemented with 10 mM MES were adjusted to the desired pH and roots of 5 days old seedlings were analyzed as described above.

Mating-based split-ubiquitin system (mbSUS) measurements

For the mbSUS the coding sequences of *CNGC10*, *AHA2*, *BAK1* and *BRI1* were either fused to the sequences coding for the C-terminal part of ubiquitin (Cub) or the N-terminal part of ubiquitin (Nub). Namely, the plasmids pMetYC (Cub) and pXNubA22 (Nub) were used (**Grefen et al., 2009**). pNubWt-Xgate (**Obrdlik et al., 2004**) and the empty pXNubA22 vector served as positive and negative control, respectively. The experiments were performed as described by **Grefen** (**2014**) with some modifications: After dropping the mated yeasts on yeast extract peptone dextrose (YPD) plates they were scratched off with pipette tips, resuspended in 100 µl H_2O and 5 µl were transferred to complete supplement mixture (CSM)-Leu -Trp -Ura -Met plates. The growth assay was performed with adjusted optical density of the yeast cultures in one dilution. Here, vector selective plates (CSM-Leu -Trp -Ura -Met) or interaction selective plates (CSM-Leu -Trp -Ura -Met, -Ade, -His) with 5 µM and 500 µM methionine were used. The growth of the yeast was documented after 72 h of incubation at 28 °C.

FRET-FLIM analysis

For FRET-FLIM analysis, the coding sequences were expressed as C-terminal fluorophore fusions, using pH7FWG2 (GFP), pB7RWG2 (RFP) or pABind-mCherry (**Karimi et al., 2002**; **Bleckmann et al., 2010**). These binary vectors and *p19* as gene silencing suppressor were transformed into *Agrobacterium tumefaciens* strain GV3101 and infiltrated into *Nicotiana benthamiana* leaves. The measurements were performed 2 to 3 days after infiltration using a SP8 laser scanning microscope (Leica Microsystems GmbH) with LAS AF and SymPhoTime (PicoQuant) software as described (**Veerabagu et al., 2012**). Before performing the FRET-FLIM measurement, the presence of the fluorophores was imaged by using 488 nm or 561 nm lasers for GFP or RFP excitation, respectively. The fluorescence lifetime τ [ns] of either the donor only expressing cells or the cells expressing the indicated combinations was measured with a pulsed laser as an excitation light source with 470 nm and a repetition rate of 40 MHz (PicoQuant Sepia Multichannel Picosecond Diode Laser, PicoQuant Time-

harp 260 TCSPC Module and Picosecond Event Timer). The acquisition was performed until 500 photons in the brightest pixel were reached. To obtain the GFP fluorescence lifetime, data processing was performed with SymPhoTime software and bi-exponential curve fitting and correction for the instrument response function.

Statistics

If not otherwise indicated, for calculation of average, standard error (SE) and standard deviation (SD) Excel v1809 or SAS JMP 14 were used. For small sample numbers the 2-sample t-test was chosen (***De Winter, 2013***).

pH time-course measurements

As the time-course measurements of the BL response were normalized to the control measurements, the standard deviations of treatment and control were added quadratically for each time point and replicate before averaging to calculate the combined standard deviation of all replicates, which is used to compute the standard error.

Computational Methods

Model Setup

The model consisting of ordinary differential equations was constructed in COPASI (***Hoops et al., 2006***; ***Mendes et al., 2009***) 4.30, build 240, running on a 64-bit machine with Windows 8. Reactions were defined as mass action or Michaelis Menten kinetics where appropriate (see Appendix 1 Table 3). Compartment sizes and parameters were defined based on experimental data if possible (Appendix 1 Tables 1 & 3). Unknown parameters were determined by parameter estimation. The schematic of the model was drawn using VANTED (***Junker et al., 2006***) and adheres to the Systems Biology Standard of Graphical Notation (SBGN) (***Novère et al., 2009***).

Parametrization

All unknown model parameters, where no or only a range of experimental information were available, were estimated. To account for parameter non-identifiabilities we generated 10 independent parameter sets by randomly sampling the starting parameter values before running the parameter estimation. Each parameter estimation run was set up using the particle swarm algorithm as implemented in COPASI 4.30 (***Hoops et al., 2006***), using 5,000 generations with a swarm size of 50 individual parameter combinations. The parameter estimation was repeated until the resulting solution had a χ^2 around 10.45.

Model Analyses

The time-course simulations were run deterministically using the LSODA algorithm as implemented in COPASI. The impact of different BIR3 concentrations was analyzed using the parameter scan task in COPASI to simulate the time course of the pH over the time frame of 20 min. The scaled sensitivities of the extracellular pH change in response to changes in model parameters were calculated as

534 $scaled\ sensitivity = \frac{ln(delta\ pH)}{ln(P_i)}$ at 5 min and 60 min. Results were plotted using R (***R Core Team, 2020***).

535

536 Acknowledgments

537 The research in our laboratories is supported by the German Research Foundation (DFG) with
538 grants to K.H., K.S. and U.K. (CRC 1101-A02/D02) and grants for scientific equipment (INST 37/819-
539 1 FUGG, INST 37/965-1 FUGG, INST 37/991-1 FUGG, INST 37/992-1 FUGG). We also would like to
540 thank the Schmeil Foundation and the Joachim Herz Stiftung for their support of R.G. In addition,
541 we are grateful for the support by Tom Denyer, ZMBP - University of Tübingen, for his help in the
542 interpretation of the scRNA-Seq data.

543 References

544 **Allen HR**, Ptashnyk M. Mathematical modelling and analysis of the brassinosteroid and gibberellin signalling
545 pathways and their interactions. Journal of Theoretical Biology. 2017 nov; 432:109–131. https://www.
546 sciencedirect.com/science/article/pii/S002251931730379X?via{%}3Dihub, doi: 10.1016/J.JTBI.2017.08.013.

547 **Baekgaard L**, Fuglsang AT, Palmgren MG. Regulation of plant plasma membrane H+- and Ca2+-ATPases
548 by terminal domains. J Bioenerg Biomembr. 2005 dec; 37(6):369–374. http://link.springer.com/10.1007/
549 s10863-005-9473-0http://www.ncbi.nlm.nih.gov/pubmed/16691467, doi: 10.1007/s10863-005-9473-0.

550 **Bairoch A**, Apweiler R, Wu CH, Barker WC, Boeckmann B, Ferro S, Gasteiger E, Huang H, Lopez R, Magrane M,
551 et al. The universal protein resource (UniProt). Nucleic acids research. 2005; 33(suppl_1):D154–D159.

552 **Band LR**, Wells DM, Fozard JA, Ghetiu T, French AP, Pound MP, Wilson MH, Yu L, Li W, Hijazi HI, Oh J, Pearce
553 SP, Perez-Amador MA, Yun J, Kramer E, Alonso JM, Godin C, Vernoux T, Hodgman TC, Pridmore TP, et al.
554 Systems analysis of auxin transport in the Arabidopsis root apex. The Plant cell. 2014 mar; 26(3):862–
555 75. http://www.ncbi.nlm.nih.gov/pubmed/24632533http://www.pubmedcentral.nih.gov/articlerender.fcgi?artid=
556 PMC4001398, doi: 10.1105/tpc.113.119495.

557 **Barbez E**, Dünser K, Gaidora A, Lendl T, Busch W. Auxin steers root cell expansion via apoplastic pH regulation
558 in Arabidopsis thaliana. Proceedings of the National Academy of Sciences. 2017; 114(24):E4884–E4893.

559 **Bleckmann A**, Weidtkamp-Peters S, Seidel CAM, Simon R. Stem Cell Signaling in Arabidopsis Re-
560 quires CRN to Localize CLV2 to the Plasma Membrane. PLANT PHYSIOLOGY. 2010 jan; 152(1):166–
561 176. http://www.ncbi.nlm.nih.gov/pubmed/19933383http://www.pubmedcentral.nih.gov/articlerender.fcgi?
562 artid=PMC2799354http://www.plantphysiol.org/cgi/doi/10.1104/pp.109.149930, doi: 10.1104/pp.109.149930.

563 **Borsics T**, Webb D, Andeme-Ondzighi C, Staehelin LA, Christopher DA. The cyclic nucleotide-gated calmodulin-
564 binding channel AtCNGC10 localizes to the plasma membrane and influences numerous growth responses
565 and starch accumulation in Arabidopsis thaliana. Planta. 2007; 225(3):563–573.

566 **Caesar K**, Elgass K, Chen Z, Huppenberger P, Witthöft J, Schleifenbaum F, Blatt MR, Oecking C, Harter K. A fast
567 brassinolide-regulated response pathway in the plasma membrane of Arabidopsis thaliana. The Plant jour-
568 nal : for cell and molecular biology. 2011 may; 66(3):528–40. http://www.ncbi.nlm.nih.gov/pubmed/21255166,
569 doi: 10.1111/j.1365-313X.2011.04510.x.

570 **Christopher DA**, Borsics T, Yuen CY, Ullmer W, Andème-Ondzighi C, Andres MA, Kang BH, Staehelin LA. The
571 cyclic nucleotide gated cation channel AtCNGC 10 traffics from the ER via Golgi vesicles to the plasma mem-
572 brane of Arabidopsis root and leaf cells. BMC Plant Biology. 2007; 7:1–13. doi: 10.1186/1471-2229-7-48.

Clouse SD. Brassinosteroid signal transduction: clarifying the pathway from ligand perception to gene expression. Molecular cell. 2002 nov; 10(5):973–82. http://www.ncbi.nlm.nih.gov/pubmed/12453407.

Clouse SD. Brassinosteroid signal transduction: from receptor kinase activation to transcriptional networks regulating plant development. The Plant cell. 2011 apr; 23(4):1219–30. http://www.pubmedcentral.nih.gov/articlerender.fcgi?artid=3101532{&}tool=pmcentrez{&}rendertype=abstract, doi: 10.1105/tpc.111.084475.

De Winter JC. Using the Student's t-test with extremely small sample sizes. Practical Assessment, Research, and Evaluation. 2013; 18(1):10.

Degtyarenko K, De Matos P, Ennis M, Hastings J, Zbinden M, McNaught A, Alcántara R, Darsow M, Guedj M, Ashburner M. ChEBI: a database and ontology for chemical entities of biological interest. Nucleic acids research. 2007; 36(suppl_1):D344–D350.

Duszyn M, Świeżawska B, Szmidt-Jaworska A, Jaworski K. Cyclic nucleotide gated channels (CNGCs) in plant signalling—Current knowledge and perspectives. Journal of Plant Physiology. 2019; 241:153035. https://www.sciencedirect.com/science/article/pii/S017616171930152X, doi: https://doi.org/10.1016/j.jplph.2019.153035.

Elgass K, Caesar K, Schleifenbaum F, Stierhof YD, Meixner AJ, Harter K. Novel Application of Fluorescence Lifetime and Fluorescence Microscopy Enables Quantitative Access to Subcellular Dynamics in Plant Cells. PLoS ONE. 2009 may; 4(5):e5716. http://dx.plos.org/10.1371/journal.pone.0005716, doi: 10.1371/journal.pone.0005716.

van Esse GW, Harter K, de Vries SC. Computational modelling of the BRI1 receptor system. Plant, cell & environment. 2013 sep; 36(9):1728–37. http://www.ncbi.nlm.nih.gov/pubmed/23421559, doi: 10.1111/pce.12077.

van Esse GW, van Mourik S, Stigter H, ten Hove Ca, Molenaar J, de Vries SC. A mathematical model for BRASSINOSTEROID INSENSITIVE1-mediated signaling in root growth and hypocotyl elongation. Plant physiology. 2012 sep; 160(1):523–32. http://www.pubmedcentral.nih.gov/articlerender.fcgi?artid=3440225{&}tool=pmcentrez{&}rendertype=abstract, doi: 10.1104/pp.112.200105.

van Esse G, Westphal AH, Surendran RP, Albrecht C, van Veen B, Borst JW, de Vries SC. Quantification of the brassinosteroid insensitive1 receptor in planta. Plant physiology. 2011 aug; 156(4):1691–700. http://www.pubmedcentral.nih.gov/articlerender.fcgi?artid=3149942{&}tool=pmcentrez{&}rendertype=abstract, doi: 10.1104/pp.111.179309.

van Esse W, van Mourik S, Albrecht C, van Leeuwen J, de Vries S. A mathematical model for the coreceptors SOMATIC EMBRYOGENESIS RECEPTOR-LIKE KINASE1 and SOMATIC EMBRYOGENESIS RECEPTOR-LIKE KINASE3 in BRASSINOSTEROID INSENSITIVE1-mediated signaling. Plant physiology. 2013 nov; 163(3):1472–81. http://www.ncbi.nlm.nih.gov/pubmed/24072582, doi: 10.1104/pp.113.222034.

Fasano JM, Swanson SJ, Blancaflor EB, Dowd PE, Kao Th, Gilroy S. Changes in Root Cap pH Are Required for the Gravity Response of the Arabidopsis Root. The Plant Cell. 2001; 13(4):907–921. http://www.plantcell.org/content/13/4/907, doi: 10.1105/tpc.13.4.907.

Friedrichsen DM. Brassinosteroid-Insensitive-1 Is a Ubiquitously Expressed Leucine-Rich Repeat Receptor Serine/Threonine Kinase. PLANT PHYSIOLOGY. 2000 aug; 123(4):1247–1256. http://www.plantphysiol.org/content/123/4/1247.long, doi: 10.1104/pp.123.4.1247.

Fuglsang AT, Kristensen A, Cuin TA, Schulze WX, Persson J, Thuesen KH, Ytting CK, Oehlenschlæger CB, Mahmood K, Sondergaard TE, et al. Receptor kinase-mediated control of primary active proton pumping at the plasma membrane. The Plant Journal. 2014; 80(6):951–964.

Glöckner N, Oven-Krockhaus Sz, Rohr L, Wackenhut F, Burmeister M, Wanke F, Holzwart E, Meixner AJ, Wolf S, Harter K. Three-fluorophore FRET enables the analysis of ternary protein association in living plant cells. bioRxiv. 2020; https://www.biorxiv.org/content/early/2020/10/26/722124, doi: 10.1101/722124.

Grefen C. The split-ubiquitin system for the analysis of three-component interactions. In: *Arabidopsis Protocols* Springer; 2014.p. 659–678.

Grefen C, Obrdlik P, Harter K. The determination of protein-protein interactions by the mating-based split-ubiquitin system (mbSUS). In: *Plant Signal Transduction* Springer; 2009.p. 217–233.

Großeholz R, Feldman-Salit A, Wanke F, Schulze S, Glöckner N, Kemmerling B, Harter K, Kummer U. Specifying the role of BAK1-interacting receptor-like kinase 3 in brassinosteroid signaling. Journal of Integrative Plant Biology. 2020; 62(4). doi: 10.1111/jipb.12803.

Hacham Y, Holland N, Butterfield C, Ubeda-Tomas S, Bennett MJ, Chory J, Savaldi-Goldstein S. Brassinosteroid perception in the epidermis controls root meristem size. Development. 2011; 138(5):839–848.

Higinbotham N. Electropotentials of plant cells. Annual Reviews of Plant Physiology. 1973; .

Hohmann U, Santiago J, Nicolet J, Olsson V, Spiga FM, Hothorn LA, Butenko MA, Hothorn M. Mechanistic basis for the activation of plant membrane receptor kinases by SERK-family coreceptors. Proceedings of the National Academy of Sciences. 2018 mar; 115(13):201714972. http://www.pnas.org/lookup/doi/10.1073/pnas.1714972115http://www.ncbi.nlm.nih.gov/pubmed/29531026http://www.pubmedcentral.nih.gov/articlerender.fcgi?artid=PMC5879659, doi: 10.1073/pnas.1714972115.

Holzheu P, Großeholz R, Kummer U. Impact of explicit area scaling on kinetic models involving multiple compartments. BMC bioinformatics. 2021; 22(1):1–12.

Holzheu P, Kummer U. Computational systems biology of cellular processes in Arabidopsis thaliana: an overview. Cellular and Molecular Life Sciences. 2020; 77(3):433–440. https://doi.org/10.1007/s00018-019-03379-9, doi: 10.1007/s00018-019-03379-9.

Holzwart E, Huerta AI, Glöckner N, Gómez BG, Wanke F, Augustin S, Askani JC, Schürholz AK, Harter K, Wolf S. BRI1 controls vascular cell fate in the Arabidopsis root through RLP44 and phytosulfokine signaling. Proceedings of the National Academy of Sciences. 2018; 115(46):11838–11843.

Hoops S, Sahle S, Gauges R, Lee C, Pahle J, Simus N, Singhal M, Xu L, Mendes P, Kummer U. COPASI–a COmplex PAthway SImulator. Bioinformatics (Oxford, England). 2006 dec; 22(24):3067–74. http://www.ncbi.nlm.nih.gov/pubmed/17032683, doi: 10.1093/bioinformatics/btl485.

Hübner K, Sahle S, Kummer U. Applications and trends in systems biology in biochemistry. The FEBS journal. 2011 aug; 278(16):2767–857. http://www.ncbi.nlm.nih.gov/pubmed/21707921, doi: 10.1111/j.1742-4658.2011.08217.x.

Imkampe J, Halter T, Huang S, Schulze S, Mazzotta S, Schmidt N, Manstretta R, Postel S, Wierzba M, Yang Y, VanDongen WM, Stahl M, Zipfel C, Goshe MB, Clouse S, de Vries SC, Tax F, Wang X, Kemmerling B. The Arabidopsis Leucine-rich Repeat Receptor Kinase BIR3 Negatively Regulates BAK1 Receptor Complex Formation and Stabilizes BAK1. The Plant Cell. 2017 aug; p. tpc.00376.2017. http://www.ncbi.nlm.nih.gov/pubmed/28842532http://www.plantcell.org/lookup/doi/10.1105/tpc.17.00376, doi: 10.1105/tpc.17.00376.

Jin Y, Jing W, Zhang Q, Zhang W. Cyclic nucleotide gated channel 10 negatively regulates salt tolerance by mediating Na+ transport in Arabidopsis. Journal of plant research. 2015; 128(1):211–220.

Junker BH, Klukas C, Schreiber F. VANTED: A system for advanced data analysis and visualization in the context of biological networks. BMC Bioinformatics. 2006; 7(1):109. http://bmcbioinformatics.biomedcentral.com/articles/10.1186/1471-2105-7-109http://www.pubmedcentral.nih.gov/articlerender.fcgi?artid=1413562{&}tool=pmcentrez{&}rendertype=abstract{%}5Cnhttp://www.biomedcentral.com/1471-2105/7/109/abstract{%}5Cninternal-pdf://160/109, doi: 10.1186/1471-2105-7-109.

657 **Karimi M**, Inzé D, Depicker A. GATEWAY vectors for Agrobacterium-mediated plant transformation. Trends in
658 plant science. 2002 may; 7(5):193–5. http://www.ncbi.nlm.nih.gov/pubmed/11992820.

659 **Kinoshita T**, Caño-Delgado A, Seto H. Binding of brassinosteroids to the extracellular domain of plant recep-
660 tor kinase BRI1. Nature. 2005; 433(13):167–171. http://www.nature.com/nature/journal/v433/n7022/abs/
661 nature03227.html, doi: 10.1038/nature03188.Published.

662 **Ladwig F**, Dahlke RI, Stührwohldt N, Hartmann J, Harter K, Sauter M. Phytosulfokine Regulates
663 Growth in Arabidopsis through a Response Module at the Plasma Membrane That Includes CYCLIC
664 NUCLEOTIDE-GATED CHANNEL17, H + -ATPase, and BAK1. The Plant Cell. 2015 jun; 27(6):1718–
665 1729. http://www.ncbi.nlm.nih.gov/pubmed/26071421http://www.pubmedcentral.nih.gov/articlerender.fcgi?
666 artid=PMC4498212http://www.plantcell.org/lookup/doi/10.1105/tpc.15.00306, doi: 10.1105/tpc.15.00306.

667 **Lv M**, Li J. Molecular Mechanisms of Brassinosteroid-Mediated Responses to Changing Environments in Ara-
668 bidopsis. International Journal of Molecular Sciences. 2020 Apr; 21(8):2737. http://dx.doi.org/10.3390/
669 ijms21082737, doi: 10.3390/ijms21082737.

670 **Lv M**, Li M, Chen W, Wang Y, Sun C, Yin H, He K, Li J. Thermal-enhanced bri1-301 instability reveals a plasma
671 membrane protein quality control system in plants. Frontiers in plant science. 2018; 9:1620.

672 **Ma X**, Denyer T, Timmermans MC. PscB: A Browser to Explore Plant Single Cell RNA-Sequencing Datasets. Plant
673 Physiology. 2020; 183(2):464–467.

674 **Maathuis FJ**, Sanders D. Energization of potassium uptake in Arabidopsis thaliana. Planta. 1993; 191(3):302–
675 307.

676 **Mendes P**, Hoops S, Sahle S, Gauges R, Dada J, Kummer U. Computational modeling of biochemical networks
677 using COPASI. In: *Systems Biology* Springer; 2009.p. 17–59.

678 **Merlot S**, Leonhardt N, Fenzi F, Valon C, Costa M, Piette L, Vavasseur A, Genty B, Boivin K, Müller A, et al. Consti-
679 tutive activation of a plasma membrane H+-ATPase prevents abscisic acid-mediated stomatal closure. The
680 EMBO journal. 2007; 26(13):3216–3226.

681 **Minami A**, Takahashi K, Inoue Si, Tada Y, Kinoshita T. Brassinosteroid induces phosphorylation of the plasma
682 membrane H+-ATPase during hypocotyl elongation in Arabidopsis thaliana. Plant and Cell Physiology. 2019;
683 60(5):935–944.

684 **Müssig C**, Fischer S, Altmann T. Brassinosteroid-regulated gene expression. Plant physiology. 2002
685 jul; 129(3):1241–51. http://www.ncbi.nlm.nih.gov/pubmed/12114578http://www.pubmedcentral.nih.
686 gov/articlerender.fcgi?artid=PMC166518http://www.ncbi.nlm.nih.gov/pubmed/12114578{%}5Cnhttp:
687 //www.pubmedcentral.nih.gov/articlerender.fcgi?artid=PMC166518, doi: 10.1104/pp.011003.

688 **Newman I**. Ion transport in roots: measurement of fluxes using ion-selective microelectrodes to characterize
689 transporter function. Plant, cell & environment. 2001; 24(1):1–14.

690 **Novère NL**, Hucka M, Mi H, Moodie S, Schreiber F, Sorokin A, Demir E, Wegner K, Aladjem MI, Wimalaratne
691 SM, Bergman FT, Gauges R, Ghazal P, Kawaji H, Li L, Matsuoka Y, Villéger A, Boyd SE, Calzone L, Courtot
692 M, et al. The Systems Biology Graphical Notation. Nature Biotechnology. 2009 aug; 27(8):735–741. http:
693 //www.nature.com/doifinder/10.1038/nbt.1558, doi: 10.1038/nbt.1558.

694 **Obrdlik P**, El-Bakkoury M, Hamacher T, Cappellaro C, Vilarino C, Fleischer C, Ellerbrok H, Kamuzinzi R, Ledent
695 V, Blaudez D, et al. K+ channel interactions detected by a genetic system optimized for systematic studies
696 of membrane protein interactions. Proceedings of the National Academy of Sciences. 2004; 101(33):12242–
697 12247.

Oh MH, Wang X, Clouse SD, Huber SC. Deactivation of the Arabidopsis BRASSINOSTEROID INSENSITIVE 1 (BRI1) receptor kinase by autophosphorylation within the glycine-rich loop. Proceedings of the National Academy of Sciences of the United States of America. 2012 jan; 109(1):327–32. http://www.pubmedcentral.nih.gov/articlerender.fcgi?artid=3252896{&}tool=pmcentrez{&}rendertype=abstract, doi: 10.1073/pnas.1108321109.

Pacifici E, Di Mambro R, Dello Ioio R, Costantino P, Sabatini S. Acidic cell elongation drives cell differentiation in the Arabidopsis root. The EMBO journal. 2018; 37(16):e99134.

Palmgren MG, Sommarin M, Serrano R, Larsson C. Identification of an autoinhibitory domain in the C-terminal region of the plant plasma membrane H+-ATPase. Journal of Biological Chemistry. 1991; 266(30):20470–20475.

Phyo P, Gu Y, Hong M. Impact of acidic pH on plant cell wall polysaccharide structure and dynamics: insights into the mechanism of acid growth in plants from solid-state NMR. Cellulose. 2019; 26(1):291–304. https://doi.org/10.1007/s10570-018-2094-7, doi: 10.1007/s10570-018-2094-7.

R Core Team. R: A Language and Environment for Statistical Computing. R Foundation for Statistical Computing, Vienna, Austria; 2020, https://www.R-project.org/.

Regenberg B, Villalba JM, Lanfermeijer FC, Palmgren MG. C-terminal deletion analysis of plant plasma membrane H(+)-ATPase: yeast as a model system for solute transport across the plant plasma membrane. The Plant cell. 1995 oct; 7(10):1655–1666. http://www.ncbi.nlm.nih.gov/pubmed/7580256http://www.pubmedcentral.nih.gov/articlerender.fcgi?artid=PMC161027, doi: 10.1105/tpc.7.10.1655.

Sankar M, Osmont KS, Rolcik J, Gujas B, Tarkowska D, Strnad M, Xenarios I, Hardtke CS. A qualitative continuous model of cellular auxin and brassinosteroid signaling and their crosstalk. Bioinformatics. 2011 may; 27(10):1404–1412. https://academic.oup.com/bioinformatics/article-lookup/doi/10.1093/bioinformatics/btr158, doi: 10.1093/bioinformatics/btr158.

Staal M, De Cnodder T, Simon D, Vandenbussche F, Van Der Straeten D, Verbelen JP, Elzenga T, Vissenberg K. Apoplastic alkalinization is instrumental for the inhibition of cell elongation in the Arabidopsis root by the ethylene precursor 1-aminocyclopropane-1-carboxylic acid. Plant Physiology. 2011; 155(4):2049–2055.

Sullivan A, Purohit PK, Freese NH, Pasha A, Esteban E, Waese J, Wu A, Chen M, Chin CY, Song R, et al. An 'eFP-Seq Browser'for visualizing and exploring RNA sequencing data. The Plant Journal. 2019; 100(3):641–654.

Veerabagu M, Elgass K, Kirchler T, Huppenberger P, Harter K, Chaban C, Mira-Rodado V. The Arabidopsis B-type response regulator 18 homomerizes and positively regulates cytokinin responses. Plant Journal. 2012 dec; 72(5):721–731. http://doi.wiley.com/10.1111/j.1365-313X.2012.05101.x, doi: 10.1111/j.1365-313X.2012.05101.x.

Verbelen JP, Cnodder TD, Le J, Vissenberg K, Baluška F. The root apex of Arabidopsis thaliana consists of four distinct zones of growth activities: meristematic zone, transition zone, fast elongation zone and growth terminating zone. Plant signaling & behavior. 2006; 1(6):296–304.

Vernoux T, Brunoud G, Farcot E, Morin V, Van den Daele H, Legrand J, Oliva M, Das P, Larrieu A, Wells D, Guédon Y, Armitage L, Picard F, Guyomarc'h S, Cellier C, Parry G, Koumproglou R, Doonan JH, Estelle M, Godin C, et al. The auxin signalling network translates dynamic input into robust patterning at the shoot apex. Molecular systems biology. 2011 jan; 7(508):508. http://www.pubmedcentral.nih.gov/articlerender.fcgi?artid=3167386{&}tool=pmcentrez{&}rendertype=abstract, doi: 10.1038/msb.2011.39.

Vukasinovic N, Wang Y, Vanhoutte I, Fendrych M, Guo B, Kvasnica M, Jiroutova P, Oklestkova J, Strnad M, Russinova E. Local brassinosteroid biosynthesis enables optimal root growth. bioRxiv. 2020; .

Wang J, Jiang J, Wang J, Chen L, Fan Sl, Wu Jw, Wang X, Wang Zx. Structural insights into the negative regulation of BRI1 signaling by BRI1-interacting protein BKI1. Cell research. 2014; 24(11):1–14. http://dx.doi.org/10.1038/cr.2014.132http://www.ncbi.nlm.nih.gov/pubmed/25331450, doi: 10.1038/cr.2014.132.

Wang Zy, Seto H, Fujioka S, Yoshida S, Chory J. BRI1 is a critical component of a plasma-membrane receptor for plant steroids. Nature. 2001; 410(MARCH):380–383.

White PJ, Biskup B, Elzenga JTM, Homann U, Thiel G, Wissing F, Maathuis FJM. Advanced patch-clamp techniques and single-channel analysis. Journal of Experimental Botany. 1999 jun; 50(Special):1037–1054. http://jxb.oxfordjournals.org/content/50/Special{_}Issue/1037.short, doi: 10.1093/jxb/50.Special_Issue.1037.

Winter D, Vinegar B, Nahal H, Ammar R, Wilson GV, Provart NJ. An "electronic fluorescent pictograph" Browser for exploring and analyzing large-scale biological data sets. PLoS ONE. 2007 aug; 2(8):e718. http://dx.plos.org/10.1371/journal.pone.0000718, doi: 10.1371/journal.pone.0000718.

Witthöft J, Caesar K, Elgass K, Huppenberger P, Kilian J, Schleifenbaum F, Oecking C, Harter K. The activation of the Arabidopsis P-ATPase 1 by the brassinosteroid receptor BRI1 is independent of threonine 948 phosphorylation. Plant Signaling & Behavior. 2011 jul; 6(7):1063–1066. http://www.landesbioscience.com/journals/psb/article/15650/, doi: 10.4161/psb.6.7.15650.

Witthöft J, Harter K. Latest news on Arabidopsis brassinosteroid perception and signaling. Frontiers in plant science. 2011 jan; 2(October):58. http://www.pubmedcentral.nih.gov/articlerender.fcgi?artid=3355717{&}tool=pmcentrez{&}rendertype=abstract, doi: 10.3389/fpls.2011.00058.

Wolf S. Deviating from the Beaten Track: New Twists in Brassinosteroid Receptor Function. International Journal of Molecular Sciences. 2020 Feb; 21(5):1561. http://dx.doi.org/10.3390/ijms21051561, doi: 10.3390/ijms21051561.

Wolf S, Van Der Does D, Ladwig F, Sticht C, Kolbeck A, Schürholz AK, Augustin S, Keinath N, Rausch T, Greiner S, et al. A receptor-like protein mediates the response to pectin modification by activating brassinosteroid signaling. Proceedings of the National Academy of Sciences. 2014; 111(42):15261–15266.

Yuan W, Li Y, Li L, Siao W, Zhang Q, Zhang Y, Liu J, Xu W, Miao R. BR-INSENSITIVE1 regulates hydrotropic response by interacting with plasma membrane H+-ATPases in Arabidopsis. Plant Signaling & Behavior. 2018; 13(8):e1486147. https://doi.org/10.1080/15592324.2018.1486147, doi: 10.1080/15592324.2018.1486147, pMID: 30067914.

Zhang X, Zhou L, Qin Y, Chen Y, Liu X, Wang M, Mao J, Zhang J, He Z, Liu L, et al. A temperature-sensitive misfolded bri1-301 receptor requires its kinase activity to promote growth. Plant Physiology. 2018; 178(4):1704–1719.

Appendix 1

Model Information

Compartments

Appendix 1 Table 1. Overview of model compartments and sizes for both MZ and early EZ. [a] calculated by multiplying the membrane area with the cell wall thickness (***van Esse et al., 2011***; ***Caesar et al., 2011***). [b] estimated volume based on cell dimensions and cellular volume (***van Esse et al., 2011***). [c] estimated surface area, included as scaling factor in the global quantities.

Root zone	Compartment	Size
Meristematic zone	cytosol	8.47×10^{-13} dm^3
	membrane	7.67×10^{-8} dm^2
	cell wall[a]	3.03×10^{-13} dm^3
	vacuole	NA
	vacuolar surface	NA
Early elongation zone	cytosol	2.271×10^{-12} dm^3
	membrane	2.098×10^{-7} dm^2
	cell wall[a]	8.2871×10^{-13} dm^3
	vacuole[b]	2.352×10^{-12} dm^3
	vacuolar surface[c]	1.087×10^{-7} dm^2

Ordinary Differential Equations

Compartment Sizes

Cell Wall Volume

$$V_{cell\ wall}(t) = A_{cell\ surface} \cdot cell\ wall\ thickness(t)$$

Model species

BRI1

$$\begin{aligned}\frac{d([BRI1] \cdot A_{cell\ surface})}{dt} = &- A_{cell\ surface} \cdot (k_{on} \cdot [BL] \cdot [BRI1] - k_{off} \cdot [BRI1\ BL]) \\ &- A_{cell\ surface} \cdot (k \cdot [BRI1] \cdot [BKI1] - k \cdot K_D \cdot [BRI1\ BKI1]) \\ &+ A_{cell\ surface} \cdot k_{off} \cdot [BRI1p\ BL] \\ &+ A_{cell\ surface} \cdot k_{off2} \cdot [BAK1\ BRI1p\ BL] \\ &+ A_{cell\ surface} \cdot k_{off2} \cdot [BAK1p\ BRI1pp\ BL] \\ &+ A_{cell\ surface} \cdot k_{off3} \cdot [BAK1p\ BRI1pppS891\ BL]\end{aligned}$$

BL

$$\frac{d([BL] \cdot A_{cell\ surface})}{dt} = - A_{cell\ surface} \cdot (k_{on} \cdot [BL] \cdot [BRI1] - k_{off} \cdot [BRI1\ BL]) + A_{cell\ surface} \cdot k_{off} \cdot [BRI1p\ BL] + A_{cell\ surface} \cdot k_{off2} \cdot [BAK1\ BRI1p\ BL] + A_{cell\ surface} \cdot k_{off2} \cdot [BAK1p\ BRI1pp\ BL] + A_{cell\ surface} \cdot k_{off3} \cdot [BAK1p\ BRI1pppS891\ BL] + V_{cell\ wall} \cdot (k \cdot dose \cdot stimulation - k \cdot [BL]$$

BKI1pY211

$$\frac{d([BKI1pY211] \cdot V_{cytosol})}{dt} = + A_{cell\ surface} * k * [BRI1\ BL] * \frac{[BKI1]}{(K_{i,BKI1} + [BKI1] * (1 + \frac{[BKI1]}{K_{i,BKI1}}) * (1 + \frac{[BIK1]}{K_{i,BIK1}})} - A_{cell\ surface} * k * [BKI1pY211]$$

BKI1

$$\frac{d([BKI1] * A_{cell\ surface})}{dt} = - A_{cell\ surface} * k * [BRI1\ BL] * \frac{[BKI1]}{(K_{i,BKI1} + [BKI1] * (1 + \frac{[BKI1]}{K_{i,BKI1}}) * (1 + \frac{[BIK1]}{K_{i,BIK1}})} + A_{cell\ surface} * k * [BKI1pY211]$$

phosphorylated AHA C-terminus

$$\frac{d([AHACTp] \cdot A_{cell\ surface})}{dt} = - A_{cell\ surface} \cdot k \cdot [AHACTp] + A_{cell\ surface} \cdot k \cdot [BAK1p\ BRI1pp\ BL] \cdot \frac{[AHACT]}{[AHACT] + K}$$

AHA C-terminus

$$\frac{d([AHACT] \cdot A_{cell\ surface})}{dt} = + A_{cell\ surface} \cdot k \cdot [AHACTp] - A_{cell\ surface} \cdot k \cdot [BAK1p\ BRI1pp\ BL] \cdot \frac{[AHACT]}{[AHACT] + K}$$

BAK1

$$\frac{d([BAK1] \cdot A_{cell\ surface})}{dt} = - A_{cell\ surface} \cdot (k \cdot [BAK1] \cdot [BIR3] - k \cdot K_D \cdot [BIR3\ BAK1]) - A_{cell\ surface} \cdot (k \cdot [BAK1] \cdot [BRI1p\ BL] - k \cdot K_D \cdot [BAK1\ BRI1p\ BL]) + A_{cell\ surface} \cdot k_{off2} \cdot [BAK1\ BRI1p\ BL] + A_{cell\ surface} \cdot k_{off2} \cdot [BAK1p\ BRI1pp\ BL] + A_{cell\ surface} \cdot k_{off3} \cdot [BAK1p\ BRI1pppS891\ BL]$$

BAK1 BRI1p BL

$$\frac{d([BAK1\ BRI1p\ BL] \cdot A_{cell\ surface})}{dt} = + A_{cell\ surface} \cdot (k \cdot [BRI1p\ BL] \cdot [BAK1] - k_{off} \cdot [BAK1\ BRI1p\ BL]) - A_{cell\ surface} \cdot k_{off2} \cdot [BAK1\ BRI1p\ BL] - A_{cell\ surface} \cdot k \cdot [BAK1\ BRI1p\ BL]$$

BAK1p BRI1pp BL

$$\frac{d([BAK1p\ BRI1pp\ BL] \cdot A_{cell\ surface})}{dt} = + A_{cell\ surface} \cdot k \cdot [BAK1\ BRI1p\ BL] - A_{cell\ surface} \cdot k_{off2} \cdot [BAK1p\ BRI1pp\ BL] - A_{cell\ surface} \cdot k \cdot [BAK1p\ BRI1pp\ BL] \cdot \frac{[BAK1p\ BRI1pp\ BL]}{[BAK1p\ BRI1pp\ BL] + K_M}$$

BAK1p BRI1pppS891 BL

$$\frac{d([BAK1p\ BRI1pppS891\ BL] \cdot A_{cell\ surface})}{dt} = + A_{cell\ surface} \cdot k \cdot [BAK1p\ BRI1pp\ BL] \cdot \frac{[BAK1p\ BRI1pp\ BL]}{[BAK1p\ BRI1pp\ BL] + K_M} - A_{cell\ surface} \cdot k_{off3} \cdot [BAK1p\ BRI1pppS891\ BL]$$

BIK1

$$\frac{d([BIK1] \cdot A_{cell\ surface})}{dt} = - A_{cell\ surface} \cdot k \cdot [BRI1\ BL] \cdot \frac{[BIK1]}{(K_{i,BIK1} + [BIK1] \cdot (1 + \frac{[BKI1]}{K_{i,BKI1}}) \cdot (1 + \frac{[BIK1]}{K_{i,BIK1}})} + A_{cell\ surface} \cdot k \cdot [BIK1p]$$

BIK1p

$$\frac{d([BIK1p] \cdot A_{cell\ surface})}{dt} = + A_{cell\ surface} \cdot k \cdot [BRI1\ BL] \cdot \frac{[BIK1]}{(K_{i,BIK1} + [BIK1] \cdot (1 + \frac{[BKI1]}{K_{i,BKI1}}) \cdot (1 + \frac{[BIK1]}{K_{i,BIK1}})} - A_{cell\ surface} \cdot k \cdot [BIK1p]$$

BRI1 BL

$$\frac{d([BRI1\ BL] \cdot A_{cell\ surface})}{dt} = - A_{cell\ surface} \cdot k \cdot [BRI1\ BL] \cdot \frac{[1]}{(1 + \frac{[BKI1]}{K_{i,BKI1}}) \cdot (1 + \frac{[BIK1]}{K_{i,BIK1}})} + A_{cell\ surface} \cdot (k \cdot stimulation \cdot [BL] \cdot [BRI1] - k_{off} \cdot [BRI1\ BL])$$

BRI1p BL

$$\frac{d([BRI1p\ BL] \cdot A_{cell\ surface})}{dt} = + A_{cell\ surface} \cdot k \cdot [BRI1\ BL] \cdot \frac{[1]}{(1 + \frac{[BKI1]}{K_{i,BKI1}}) \cdot (1 + \frac{[BIK1]}{K_{i,BIK1}})} - {}_{cell\ surface} \cdot (k \cdot [BAK1] \cdot [BRI1p\ BL] - k_{off} \cdot [BAK1\ BRI1p\ BL]) - A_{cell\ surface} \cdot k_{off} \cdot [BRI1p\ BL]$$

BIR3

$$\frac{d([BIR3] \cdot A_{cell\ surface})}{dt} = - A_{cell\ surface} \cdot (k \cdot [BIR3] \cdot [BAK1] - k \cdot K_D \cdot [BIR3\ BAK1]) - A_{cell\ surface} \cdot (k \cdot [BIR3] \cdot [BRI1] - k \cdot K_D \cdot [BIR3\ BRI1])$$

BIR3 BAK1

$$\frac{d([BIR3\ BAK1] \cdot A_{cell\ surface})}{dt} = - A_{cell\ surface} \cdot (k \cdot [BIR3] \cdot [BAK1] - k \cdot K_D \cdot [BIR3\ BAK1])$$

BIR3 BRI1

$$\frac{d([BIR3\ BRI1] \cdot A_{cell\ surface})}{dt} = -A_{cell\ surface} \cdot (k \cdot [BIR3] \cdot [BRI1] - k \cdot K_D \cdot [BIR3\ BRI1])$$

Extracellular Proton Concentration

$$\frac{d([H^+_{out}] \cdot V_{cell\ wall})}{dt} = +A_{cell\ surface} \cdot k \cdot [AHA] \cdot [H^+_{in}] \cdot \frac{[AHA]}{[AHA] + Inhibition_{AHACT} \cdot [AHACT]} - A_{cell\ surface} \cdot k \cdot ([H^+_{out}] - [H^+_{in}])$$

CNGC10 open

$$\frac{d([CNGC10_{open}] \cdot A_{cell\ surface})}{dt} = +A_{cell\ surface} \cdot \left(k_1 \cdot [BAK1p\ BRI1pp\ BL] \cdot \frac{[CNGC10_{closed}]}{K_M + [CNGC10_{closed}]} - k_2 \cdot [CNGC10_{open}]\right)$$

CNGC10 closed

$$\frac{d([CNGC10_{closed}] \cdot A_{cell\ surface})}{dt} = -A_{cell\ surface} \cdot \left(k_1 \cdot [BAK1p\ BRI1pp\ BL] \cdot \frac{[CNGC10_{closed}]}{K_M + [CNGC10_{closed}]} - k_2 \cdot [CNGC10_{open}]\right)$$

Intracellular Potassium Concentration

$$\frac{d([K^+_{in}] \cdot V_{cell})}{dt} = +k \cdot A_{cell\ surface} \cdot [CNGC10_{open}] \cdot \frac{[K^+_{out}]}{K_d} \cdot \left(\frac{E_m}{-0.59} - 1\right) + A_{cell\ surface} \cdot k \cdot [K^+_{in}] - k \cdot K_{eq} \cdot [K^+_{ex}]) - A_{vacuole} \cdot k \cdot (K^+_{in} - K^+_{vac})$$

Vacuolar Potassium Concentration

$$\frac{d([K^+_{vac}] \cdot V_{vacuole})}{dt} = +A_{vacuole} \cdot k \cdot ([K^+_{in}] - [K^+_{vac}])$$

Global Quantities

Net charge change

$$\triangle Q = (([K^+_{in}] - [K^+_{in,0}]) \cdot V_{cell} - ([H^+_{out}] - [H^+_{out,0}]) \cdot V_{cell\ wall}) \cdot Faraday\ constant\ F \cdot factor_{pmol\ to\ mol}$$

$$with: \ F = 96485.33212 C\ mol^{-1}$$

Membrane potential change

$$\triangle E_m = \frac{net\ charge\ distribution\ change\ \triangle Q}{specific\ capacitance * membrane\ area}$$

Cell wall instability

$$cell\ wall\ instability(t) = \frac{1}{1 + e^{-0.001\left([H^+_{out}]-1.2\cdot proton\ readout\right)}} \cdot stimulation \cdot \left(1 - \frac{1}{1 + e^{-10^7\cdot\left(cell\ wall(t)-5.0\cdot10^{-6}\right)}}\right)$$

Cell wall thickness

$$\frac{d(cell\ wall\ thickness)}{dt} = 0.00015 \cdot stimulation \cdot cell\ wall\ thickness(t)$$

factor BIR3

Factor representing the expression level of BIR3. 1 represents the normal expression level, 100 represents the overexpression level.

factor BRI1

Factor representing the expression level of BRI1. 1 represents the normal expression level, 130 represents the overexpression level.

Events

Stimulation

Trigger: $Model\ Time > 86400\ s$

Target: Global quantity $stimulation\ transient\ value$ is set to 1 from the initial value of 0.

Overview of model components

Appendix 1 Table 2. Protein are specified by the Uniprot identifier (***Bairoch et al., 2005***) and the corresponding gene ID. For ions and chemical compounds, the ChEBI (Chemical Entities of Biological Interest (***Degtyarenko et al., 2007***)) identifier is used instead. The initial concentrations of all un-phosphorylated species and complexes between proteins were set to 0 pM.

Species	Uniprot ID / ChEBI ID	Gene ID	Initial Concentration	Source
BRI1	O22476	At4g39400	$0.182\,633$ pM	(***van Esse et al., 2011***)
BAK1	Q94F62	At4g33430	$0.099\,632$ pM	(***van Esse et al., 2011***)
BIR3			$0.237\,423\,11$ pM	this study
AHA			$0.232\,442$ pM	$AHA1 + AHA2$
AHA1	P20649	At2g18960	$0.116\,221$ pM	assumption: $\frac{AHA1}{AHA2} \approx \frac{1}{1}$ mRNA data (eFP Browser) (***Winter et al., 2007***)
AHA2	P19456	At4g30190	$0.116\,221$ pM	this study
AHA C-terminus			$0.232\,442$ pM	$AHA1 + AHA2$
BKI1	Q9FMZ0	At5g42750	$0.219\,16$ pM	assumption: $1.2 * [BRI1]_{t=0}$
BIK1	O48814	At2g39660	$0.219\,16$ pM	assumption: $1.2 * [BRI1]_{t=0}$
$CNGC10_{closed}$	Q9LNJ0	At1g01340	0.1 pM	
H^+_{in}	24636	-	$63\,000$ pM	
H^+_{out}	24636	-	fitted to data	
K^+_{out}	29103	-	9.8425×10^9 pM	½ MS medium
K^+_{in}	29103	-	8.4×10^{10} pM	(***Maathuis and Sanders, 1993***)
K^+_{vac}	29103	-	8.4×10^{10} pM	assumed to be identical to K^+_{in}
BL	28277	-	$dose$	see experimental setup

Experimentally determined parameters

Appendix 1 Table 3. Model parameter that were either experimentally determined or where a range or estimate of experimentally determined values was available. Rate law abbreviations: MA - mass action kinetics, MM - Michaelis-Menten kinetics, CF - constant flux.

ID	Rate Law	Parameter	Value	Source
r_{01}	modified MA	K_i	up to 7.7 fold for AHA2	(***Regenberg et al., 1995***)
r_{02}	modified MA	k	0.84×10^{-9} dm s^{-1} to 1.25×10^{-9} dm s^{-1}	this study Appendix 1 Fig. 1
r_{03}	modified MA			
r_{04}	MA			
r_{05}	MA			
r_{06}	MA			
r_{07}	MA			
r_{08}	CF, MA	$dose$	0 nM, 1×10^4 pM,5×10^4 pM, 1×10^5 pM	(***Caesar et al., 2011***) this study
r_{09}	modified MA	K_d	7.4×10^3 pM to 5.5×10^4 pM	(***Clouse, 2002***) (***Hohmann et al., 2018***) (***Kinoshita et al., 2005***) (***Wang et al., 2001***)
		k_{on}	9.49×10^{-7} pMol^{-1} s^{-1}	(***Hohmann et al., 2018***)
r_{10}	modified MM	k	0.97 s^{-1}	(***Wang et al., 2014***)
r_{11}	modified MM			
r_{12}	modified MA			
r_{13}	MA			
r_{14}	MA			
r_{15}	MM			
r_{16}	MM			
r_{17}	MM	$time\ scale$	slow increase over 12 h	(***Oh et al., 2012***)
r_{d1}	MA			
r_{d2}	MA	max. k_d	1.05×10^{-2} s^{-1}	(***Hohmann et al., 2018***)
r_{d3}	MA	max. k_d	1.05×10^{-2} s^{-1}	(***Hohmann et al., 2018***)
r_{d4}	MA	$time\ scale$	residual P_i after 5 d	(***Oh et al., 2012***)
r_{d5}	MA			
r_{d6}	MA			
r_{d7}	MA			

pH measurements using pHusion

A. thaliana seedlings stably expressing SYP122-pHusion were treated with with 500 µM ortho-vanadate and the pH was measured after 30 min and 60 min based on the fluorescent ratio of mRFP and eGFP in the EZ. The measurements were conducted for n = 30 seedlings. Plants treated with MS medium were taken as control, outliers were set to pH 8.

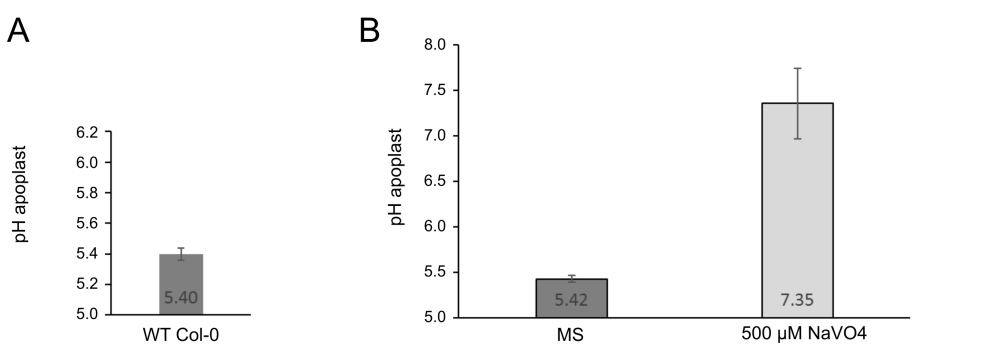

Appendix 1 Figure 1. Measurement of the proton leak flux from the cell wall using SYP122-pHusion. A. Resting pH in the EZ of the WT Col-0. Error bars represent SD (n = 3). B. pH after 1 h of treatment with $500\,\mu M$ ortho-Vanadate compared to control (MS). Error bars represent SD (n = 30). The proton leak was estimated based on the pH difference and the average size of an epidermis cell in the mid EZ (***van Esse et al., 2011***).

Example calculation of E_m and pH change

pH 5.4 → 5.0

$$\triangle[H^+]: \quad 10^{-5.0}\,M - 10^{-5.4}\,M = 1 * 10^{-5} - 3.16 * 10^{-6} M = 6.019 * 10^{-6} M$$

$$\triangle nH^+: \quad 6.019 * 10^{-6} M * 8.2892 * 10^{-13} l = 4.99 * 10^{-18} mol$$

$$\triangle Q: \quad 4.99 * 10^{-18} mol * 96485.33212 \frac{C}{mol} = 4.81 * 10^{-13} C$$

$$\triangle E_m: \quad \frac{4.81 * 10^{-13} C}{0.0081 * 2.098 * 10^{-9} m^2} = 2.83 * 10^{-2} V = 28.3 mV$$

Supporting Figures

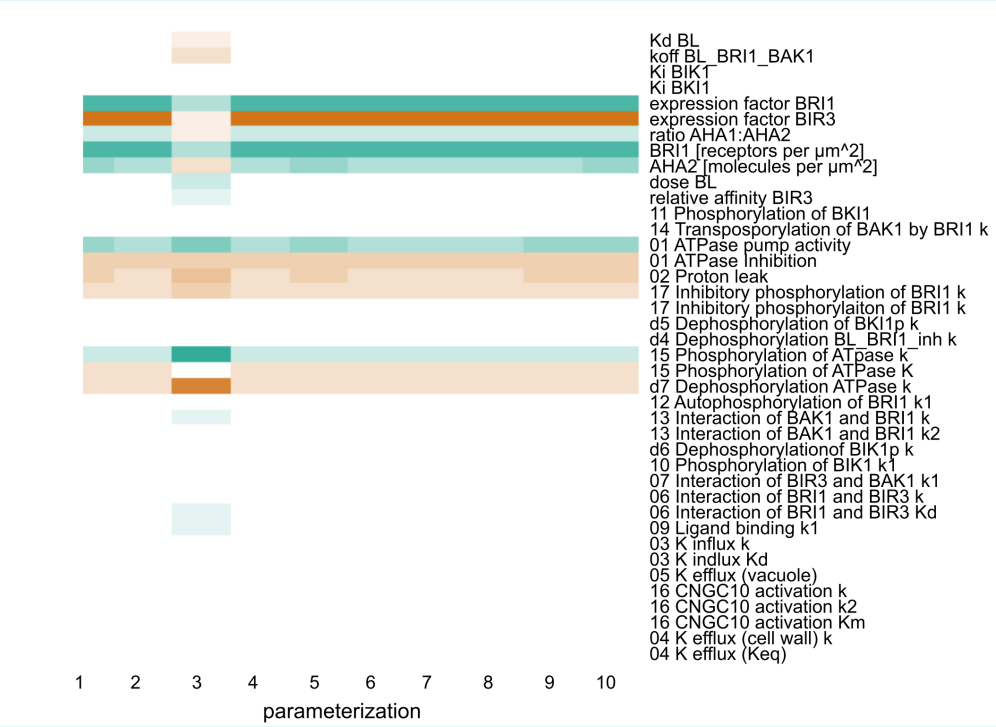

Appendix 1 Figure 2. Scaled sensitivities of the pH change 60 min after stimulation with 10 nM BL in response to changes in the parameter and global quantities values. Color code: red - negative control, white - no influence, green - positive control. Color saturation indicates strength of the influence.

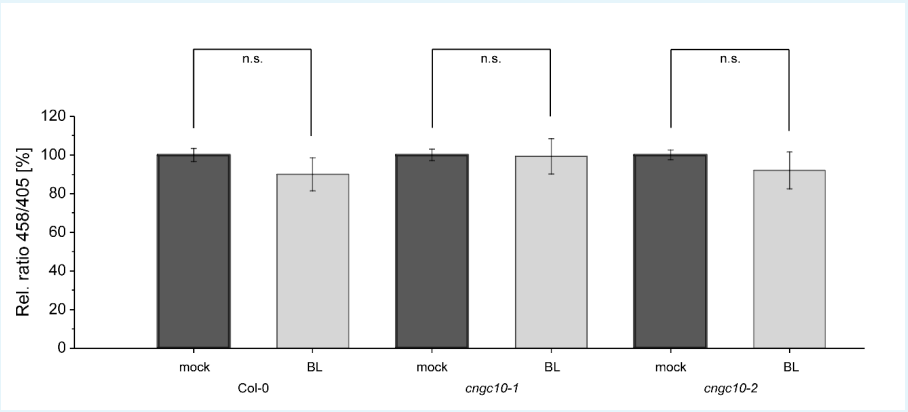

Appendix 1 Figure 3. Comparison of the relative apoplastic pH of epidermal root cells in the MZ of wild type and two independent *cngc10* mutant plants after 60 min of BL (10 nM) or mock treatment, visualized by HPTS staining. The data derived from the mock treatments of the respective line were set to 100. Error bars represent SE ($n \geq 8$). Statistical evaluations were performed as described in Fig. 7C; n.s.: not significant.